The three-dimensional structure of the tropical circulation cell in the central equatorial Pacific ocean

Renellys C. Perez[1]

William S. Kessler[1]

[1]*National Oceanic and Atmospheric Administration*

Pacific Marine Environmental Laboratory

7600 Sand Point Way NE

Seattle, WA 98115-6349

PMEL Contribution #3200

Corresponding author email address: Renellys.C.Perez@noaa.gov

Abstract

The surface limb of the tropical circulation cell in the central equatorial Pacific ocean is characterized by strong equatorial upwelling, near-surface poleward flow, and downwelling near 4° latitude. Meridional and vertical velocity fluctuations associated with tropical instability waves (TIWs) are much larger than those associated with the cell and can modify the background circulation through rectification. OGCM experiments are used to simulate the spin-up of the cell along 140°W in response to perturbed Trade winds during various phases of the annual cycle. Equatorially-modified versions of geostrophy and Ekman theory and zonal filtering isolate the large zonal scale wind-driven response. Weakening the Trades in any season rapidly weakens the cell, decreases the shear of the zonal currents, and reduces the amplitude and propagation speed of the TIWs. In boreal fall and winter when the background winds and TIWs are seasonally strong, the spin-down of the cell is equatorially asymmetric and there is clear evidence of rectification by the modified TIWs. The ageostrophic cell response is dominated by an equatorially-modified Ekman response and is essentially linear within a given season, with relatively large interseasonal differences due to nonlinear interactions with the background cell and TIWs. Cross-equatorial velocity measurements with fine meridional and temporal sampling are required to quantify the relative contributions of these two processes to the equatorial asymmetry of the cell in boreal fall and winter.

1. Introduction

Although much is known about the upper-ocean horizontal circulation along the equator between 165°E and 110°W from multi-decadal Tropical Ocean Atmosphere (TAO) horizontal velocity measurements (Hayes et al. 1991; McPhaden 1993), long-term measurements of the meridional-upwelling circulation cell in the central equatorial Pacific ocean do not exist. Our picture of the tropical circulation cell is derived primarily from models, which are only poorly constrained by observations. This cell is characterized by strong upwelling near the equator, near-surface wind-driven poleward divergence, downwelling near 3° to 5° latitude associated with the northern and southern cold tongue sea surface temperature (SST) fronts, and convergence of geostrophic flow below the surface mixed layer (left panels of Fig. 1). The cold tongue and its sharp temperature gradients are in part sustained by equatorial upwelling and meridional heat advection by the tropical circulation cell (Wyrtki 1981; Swenson and Hansen 1999; Wang and McPhaden 1999) and better understanding of the three-dimensional processes controlling cold tongue SST will lead to improved models and predictability of the coupled climate system.

Quasi-synoptic ADCP/CTD observations from repeat cruise transects have resolved the upper-ocean mean zonal currents (u) at various longitudes along the Pacific basin (Johnson and Luther 1994; Johnson et al. 2001; Johnson et al. 2002). Johnson et al. (2001, hereafter JMF) used a third-order longitudinal polynomial fit to estimate mean u along 136°W from 9 years of ADCP transects. Along 136°W, the two strongest mean eastward currents, the Equatorial Undercurrent (EUC) and the North Equatorial Countercurrent (NECC), have velocity maxima at 0°N, 110 m and 7°N, 50 m, respectively (Obs u in Fig. 1). The westward flowing South Equatorial

Current is split into southern (SECS) and northern (SECN) branches with surface maxima at 4°S and 2°N, respectively, and larger speeds north of the equator. Due to strong transient processes in the central equatorial Pacific, estimates of the relatively weak mean meridional velocity (v) could only be made by averaging over 75° longitude and 9 years. Vertical velocity (w) was computed by downward integration of the continuity equation, $\frac{\partial w}{\partial z} = -(\frac{\partial u}{\partial x} + \frac{\partial v}{\partial y})$, requiring additional smoothing of v over 2° latitude bins to estimate $\frac{\partial v}{\partial y}$. Despite large error bars associated with w (JMF), the mean picture of the tropical circulation cell that emerges is maximum equatorial upwelling at 50 m of 1.6 m/day, surface poleward flows reaching -9 cm/sec in the south and 13 cm/sec in the north, maximum downwelling at 50 m of -0.8 m/day near 4.5°S and -1.4 m/day near 8°N, and maximum equatorward flow at 85 m depth of 5 cm/sec near 1.5°S and -4 cm/sec near 3.5°N (Obs v, w in Fig. 1). The vertical banding in w below 100 m is due to the downward integration of noise in both $\frac{\partial u}{\partial x}$ and $\frac{\partial v}{\partial y}$ (JMF).

The annual and interannual evolution of zonal currents in the central equatorial Pacific have been described from analysis of data from drifters, satellites, ADCP/CTD transects, and moorings, but much less is known about the seasonal and interannual evolution of the tropical circulation cell. Yet it is likely that such variability will be found, because the observed zonal currents vary strongly at these frequencies. Zonal equatorial currents are strongest at 140°W, with peak EUC velocities in boreal summer when the EUC is shallowest (Johnson et al. 2002, hereafter JSKM) and surface flow along the equator is eastward (Reverdin et al. 1994; Bonjean and Lagerloef 2002; JSKM). The SECN peaks in boreal winter (Reverdin et al. 1994; Bonjean and Lagerloef 2002; JSKM) and NECC peaks in boreal fall (Kessler and Taft 1987; Reverdin et al. 1994; Bonjean and Lagerloef 2002; JSKM). The EUC, SECN, and NECC are all weakened under El Niño conditions, and strengthened under La Niña conditions (JSKM) when tropical instability waves (TIWs) are also most active (Baturin and Niiler 1997; Contreras 2002). TIWs, which have periods ranging from 17 to 33 days (Lyman et al. 2007) and zonal wavelengths of 1000 to 2000 km (Legeckis 1977; Qiao and Weisberg 1995), produce large westward-propagating fluctuations in velocity, temperature, salinity, and pressure fields in the equatorial Pacific cold tongue and along its northern and southern frontal boundaries.

The Tropical Instability Wave Experiment (TIWE) resolved TIW signals in u and v at 0°N, 140°W during May 1990 to June 1991 (Weisberg and Qiao 2000, hereafter WQ). A time series of w was estimated from the continuity equation using adjacent TIWE moorings with 2° zonal and 1° meridional spacing. From these measurements, WQ found that poleward divergence and equatorial upwelling were strongest when the Southeast Trades were strong (late boreal summer to fall). TIWs were excited from August to December 1990 consistent with the intensification of the SEC, and abruptly halted when passage of a Kelvin wave weakened the SEC (WQ). On the equator, WQ found that v and w TIW fluctuations covary out of phase, with amplitudes much larger than those associated with the mean tropical circulation cell (50 cm/sec at 30 m depth for v and 20 m/day at 60 m depth for w). Based on additional observations, v fluctuations associated with TIWs can be larger than 75 cm/sec (Kessler et al. 1998; Kennan and Flament 2000; Lyman et al. 2007) and the high-frequency variability induced by TIWs dominates the low-frequency variability associated with the annual cycle (Reverdin et al. 1994; Kessler et al.

1998; Bonjean and Lagerloef 2002), posing a difficult sampling problem.

In lieu of cross-equatorial obsevations showing the tropical circulation cell, models can be used to study the three-dimensional structure of the cell and the processes by which its circulation is perturbed by varying winds and TIWs. This paper uses a numerical model to describe the spin-up of the tropical circulation cell along 140°W in response to perturbed Trade winds during different phases of the seasonal cycle and different stages of TIW development. Section 2 describes the numerical model, wind experiments, equatorial geostrophic calculations introduced to separate the ageostrophic circulation from that driven by pressure gradients, and filtering applied to remove the small zonal scale TIW response from the large zonal scale response of the tropical circulation cell. Equatorially-modified Ekman transports and vertical velocity introduced in section 2 are used to interpret the ageostrophic response. Section 3 compares the anomalous circulation during times of the year when both the background Southeast Trades and TIWs are weak and strong, and also examines how the meridional structure of the ageostrophic response differs from that of the linear wind-driven response. The linearity and meridional structure of the ageostrophic response are further evaluated in section 4 and the results are summarized in section 5.

2. Numerical Experiments

The ocean general circulation model (OGCM) used in this tropical Pacific study is version 4 of the Modular Ocean Model (MOM4; Griffies et al. 2003). The model implementation closely resembles OM3.1 described by Griffies et al. (2005) and Wittenberg et al. (2006), and substantive changes are described below. The model horizontal B-grid spans the tropical Pacific from 120°E to 60°W and 40°S to 40°N with resolution of 0.625° longitude by 0.33° latitude in the waveguide. The meridional resolution gradually stretches to 1° at 40° latitude. The model has 49 z-levels with vertical spacing of 10 m in the upper 220 m, stretching to 390 m at the deepest z-level. Bottom topography is specified from the Southampton Oceanography Centre maps of ocean floor relief with maximum depth set to 5600 m. We found that the large along-stream viscosities in the waveguide produced by the original OM3.1 horizontal viscosity scheme (Large et al. 2001; Griffies et al. 2005) generated TIWs that repeated exactly from one year to the next. This scheme was therefore deemed unsuitable for analysis of modification of the tropical circulation cell by TIWs. Instead, we use an anisotropic Laplacian viscosity scheme with constant along-stream and cross-stream viscosities of 2000 m^2/sec and 1000 m^2/sec, respectively, which produces vigorous and realistic TIWs. The model is initialized from rest with temperature and salinity from the Polar Science Center Hydrographic Climatology (PHC; Steele et al. 2001) and spun up with climatological forcing (section 2a). The zonal wind experiments (section 2b) are begun on year 17 of the climatological run.

a. Climatological forcing

The climatological wind stress is generated by fitting an annual and semi-annual harmonic to QuikSCAT scatterometer monthly mean wind stress from September 1999 to August 2005 (an early version of the Risien et al. 2008 QuikSCAT climatology). The QuikSCAT climatology is available on a 0.25° longitude by 0.25° latitude grid with 2° longitude by 2° latitude loess smoothing (Schlax and Chelton

1992; Risien et al. 2008) and is bilinearly interpolated to the model grid. The high spatial resolution of the QuikSCAT climatology resolves the intense zonal bands of wind stress divergence and curl near the equator, and temporal smoothing by the harmonic fit removes small-scale noise associated with local wind coupling to TIWs (Chelton et al. 2001; Risien et al. 2008).

Radiative and turbulent surface heat fluxes used to force the climatological run are obtained from the MIT/WHOI Objectively Analyzed air-sea Fluxes (OAFlux) project for the global oceans. Monthly mean surface heat flux composites of objectively analyzed daily surface latent and sensible heat flux from January 1, 1981 to December 31, 2002 (Yu et al. 2004; Yu and Weller 2007) and International Satellite Cloud Climatology Project (ISCCP) long-wave and short-wave radiation from July 1, 1983 to December 31, 2004 (Zhang et al. 2004) provide the surface forcing. Model SST is damped to climatological SST, based on monthly Tropical Rainfall Microwave Imager (TMI) data from September 1999 to October 2005, with a 30-day time scale. A spatially-varying mean adjustment term is added to the net surface heat flux to keep the model warm pool and ITCZ from becoming too warm (less than 20 $W\ m^{-2}$ cooling in cold tongue). The adjusted net surface heat flux averaged between 5°S and 5°N compares well with the tropical Pacific annual mean surface heat flux from coupled GFDL global climate simulations and observations (Figure 6 in Wittenberg et al. 2006).

At lateral boundaries, a solid wall boundary condition is specified and model temperature and salinity are restored to PHC climatological temperature and salinity in a 15° latitude wide sponge region with 30-day damping time scale at the poleward boundary. Sea surface salinity (SSS) is everywhere relaxed to PHC SSS with a 30-day time scale and zero net salt and water flux are assumed.

Fig. 1 compares the annual mean circulation from the climatological run along 140°W (left panels) with the observed mean circulation from JMF (right panels). Mean zonal currents compare reasonably well with observed u, with adequate realism in the EUC, NECC, and both branches of the SEC. However, the mean model SECN and NECC are weaker than estimated by JMF and the model EUC core is stronger and deeper than observed. Despite large error bars associated with the JMF (v, w) estimates, the following qualitative comparisons can be made. In and below the surface limb of the northern tropical circulation cell, the magnitude of mean model v is stronger than that estimated by JMF. As found by JMF, the model $\frac{\partial w}{\partial z}$ is dominated by $-\frac{\partial v}{\partial y}$ with equatorial divergence yielding upwelling between 3°S and 3°N and off-equatorial convergence yielding downwelling in both hemispheres. However, the model's upwelling is much stronger (3.0 m/day vs. JMF's 1.6 m/day) with paired maxima at 0.7°S, 70 m and 1.3°N, 40 m, while the off-equatorial downwelling occurs equatorward of observed downwelling (maxima at -0.5 m/day at 4.3°S, 60 m and -2.1 m/day at 3.7°N, 50 m). The off-equatorial upwelling double maxima may be a nonlinear rectification by the more intense TIWs and do not occur when the model is run with the OM3.1 viscosity scheme (section 2). On the other hand, it is unclear whether this feature could have been resolved by JMF given the considerable spatio-temporal averaging and large error bars associated with w.

b. Zonal wind experiments

To analyze the response of the tropical circulation cell along 140°W to a localized weakening (strengthening) of the Trade Winds, a series of experiments are conducted which added a westerly (easterly) wind anomaly in a 15° zonal patch centered at 140°W to the climatological wind stress. The anomalous winds are imposed for 61-day periods during various phases of the seasonal cycle and different stages of TIW evolution.

The spatio-temporal structure of the zonal wind patch, $\tau_x'(x, y, t) = S(x, y)T(t)$, is chosen to isolate the response near 140°W, provide nearly uniform forcing across the waveguide (zero divergence and curl), allow Kelvin and Rossby wave adjustment to occur within the wind patch, and avoid interference from Kelvin waves reflecting off of the Galapagos Islands. The spatial structure $S(x, y)$ is constructed from hyperbolic tangents (Nonaka et al. 2002; Kroger et al. 2005) and has the form

$$S(x,y) = \frac{A}{4}\left\{\left(\tanh\frac{3(x-x_W)}{L_x} - \tanh\frac{3(x-x_E)}{L_x}\right)\left(\tanh\frac{3(y-y_S)}{L_y} - \tanh\frac{3(y-y_N)}{L_y}\right)\right\} \tag{1}$$

where $A = 0.025$ N m^{-2} ($A > 0$ for westerly wind anomaly), $L_x = 5°$, $L_y = 5°$, $x_W = 147.5°$W, $x_E = 132.5°$W, $y_S = 20°$S, and $y_N = 20°$N. The magnitude A was chosen to be typical of the QuikSCAT zonal windstress intra-annual variability (annual cycle and interannual variability filtered out) along 140°W, which ranges from 0.015 to 0.045 N m^{-2} between 20°S and 20°N (Fig. 2). The solid box in Fig. 2 indicates the region where anomalous winds are largest (approximately equal to A). The temporal evolution of the anomaly is a 45-day rectangle, tapered with 8-day sinusoids (lower panel of Fig. 2). For several comparisons in sections 3 and 4, results will be averaged over the central 45 days when the full anomaly is applied.

The zonal wind anomalies are superimposed on the climatological wind forcing and used to drive the model during three phases of the annual cycle: boreal winter (starting on 1 January), boreal spring/summer (starting on 1 May), and boreal fall (starting on 1 September). Hereafter, seasons are discussed relative to the northern hemisphere annual cycle (e.g., fall implies boreal fall). Differences between the anomaly-forced runs and climatological control runs during the same time periods are used to describe the model response to anomalous forcing (i.e., anomalous zonal velocity is defined as $u = u_{total} - u_{clim}$, where u_{total} and u_{clim} denote the anomaly-forced and climatologically-forced zonal velocity, respectively). In the control run, as in reality, TIWs are weakest from April to June, grow rapidly in late summer/fall and persist until March. Similarly, the Southeast Trades along 140°W are strong in late summer/fall and weaken in late winter (τ_x, τ_y in Fig. 3), so the timing of imposed anomalies spans the annual cycle of the Trades and the different TIW regimes.

c. Geostrophic currents near equator

We use equatorial geostrophy to obtain the pressure gradient driven part of the response to the imposed wind anomalies. Defining the anomalous dynamic height relative to 500 db to be the difference from climatology, $\Phi = \Phi_{total} - \Phi_{clim}$, the anomalous geostrophic currents (u_g, v_g) are given by (2) away from the equator and (3) along it.

$$fu_g = -g\frac{\partial \Phi}{\partial y}, \qquad fv_g = g\frac{\partial \Phi}{\partial x} \tag{2}$$

$$\beta u_g = -g\frac{\partial^2 \Phi}{\partial y^2}, \qquad \beta v_g = g\frac{\partial^2 \Phi}{\partial x \partial y} \tag{3}$$

The solutions to these two sets of equations, however, are not continuous at their juncture. To generate a continuous estimate of u_g across the equator and preserve the equatorial solution given by (3), an equatorially trapped adjustment term can be added to Φ such that its meridional gradient, $\frac{\partial \Phi}{\partial y}$, vanishes exactly at the equator (e.g., Picaut and Tournier 1991). As described in Appendix A, we introduce an additional adjustment to Φ to ensure that v_g estimated from (2) and (3) is also continuous across the equator. The resulting geostrophic currents compare well with those computed following the method of Lagerloef et al. (1999). However, Lagerloef et al. (1999) applies a Gaussian adjustment to (u_g, v_g) whereas this approach adjusts dynamic height directly. Anomalous ageostrophic currents are defined as $u_{ag} = u - u_g$ and $v_{ag} = v - v_g$ (see Table 1 for a summary of notation).

d. Equatorially-modified Ekman theory

Classical Ekman theory predicts zonal and meridional transports of the form

$$(U_e, V_e) = \left(\frac{\tau_y}{\rho f}, \frac{-\tau_x}{\rho f}\right) \tag{4}$$

while Ekman vertical velocity (w_e) is computed from the divergence of (U_e, V_e). Given the climatological winds along 140°W (Fig. 3), this simple linear formulation yields poleward transport that is stronger south of the equator and downwelling that is too strong between 2° and 5° latitude in both hemispheres. Not only is this picture inconsistent with the observed and simulated mean tropical circulation cell (Fig. 1), the solution also blows up at the equator. An equatorially-modified Ekman model (e.g., Lagerloef et al. 1999; Wittenberg 2002) adds linear wind drag to the momentum equations, leading to

$$(U_\tau, V_\tau) = \left(\frac{r_s\tau_x + f\tau_y}{\rho(f^2 + r_s^2)}, \frac{r_s\tau_y - f\tau_x}{\rho(f^2 + r_s^2)}\right) \tag{5}$$

where r_s is the vertical shear dissipation rate and w_τ is now computed from the divergence of (U_τ, V_τ). Note that the linear drag results in downwind transport close to the equator in addition to crosswind transport from the classical formulation (5). Choosing r_s^{-1} =2 day as in Wittenberg (2002) yields a linear circulation cell with strong equatorial upwelling, poleward transport that is larger north of the equator, and off-equatorial downwelling between 3° and 5° latitude in both hemispheres (Wind V, w in Fig. 3). The intensity and equatorial asymmetry of this cell increases when the Southeast Trades are strong. The linear equatorially-modified Ekman solution agrees well with 60-day low-pass filtered ageostrophic meridional transport and vertical velocity from the climatological control run (Clim V, w in Fig. 3). However, places where they differ significantly, noted especially in the northern tropical circulation cell during late summer to early spring, indicate regions where the ocean response is poorly accounted for by linear dynamics ($\Delta V, \Delta w$ in Fig. 3).

For a purely zonal wind anomaly, (U_τ, V_τ) simplify to

$$(U_\tau, V_\tau) = \left(\frac{r_s\tau'_x}{\rho(f^2 + r_s^2)}, \frac{-f\tau'_x}{\rho(f^2 + r_s^2)}\right). \tag{6}$$

By construct, $\frac{\partial\tau'_x}{\partial x}$ and $\frac{\partial\tau'_x}{\partial y}$ are zero near the equator and along 140°W (section 2b) and w_τ reduces to

$$w_\tau \approx \frac{\beta(f^2 - r_s^2)\tau'_x}{\rho(f^2 + r_s^2)^2} \tag{7}$$

which equals the meridional gradient of V_τ (lower panels of Fig. 4). For weakened Trade wind anomaly (section 2b), these modified Ekman solutions predict anomalous eastward transport, equatorial downwelling, maximum equatorward transport at 2.3° latitude ($\pm r_s/\beta$), and maximum upwelling at 4° latitude ($\pm\sqrt{3}r_s/\beta$) (Fig. 4). Both V_τ and w_τ are later used to interpret the ageostrophic response of the tropical circulation cell to imposed wind anomalies. Model statistics will also be used to test the choice of r_s.

e. Zonal filtering of TIWs

Changes to the meridional and vertical shear of the zonal currents in response to the zonal wind anomalies produce very large modifications to the amplitude of the TIW velocity fluctuations. These changes obscure the relatively small wind-driven response. Temporal filtering can be applied to remove the TIWs (as in section 2d), but this would obscure the temporal signature of the wind-driven response in these short 61-day experiments. Instead, zonal filtering is applied to separate the two signals. This approach was recently applied by Seo et al. (2007) to remove signals with zonal scales larger than 10° longitude and isolate TIWs in a model. The zonal wavelengths of the model TIWs range between 8° and 12° longitude and the nominal width of the wind patch is 15°, so a 15° zonal low-pass triangle filter is used to isolate the large zonal scale response to anomalous winds. The subscript L is used for zonally low-pass filtered fields (e.g., u_L).

3. Weakened Trades Results

a. Near-surface response

1) Spring/summer

The near-surface background circulation (u_{clim}, v_{clim} at 5 m and w_{clim} at 60 m depth) averaged over 45 days (section 2b) in spring/summer is shown in Fig. 5. At this time of year the Southeast Trades are weak (Fig. 3) and seasonally the model EUC has shoaled giving eastward surface flow along the equator (upper panel of Fig. 5). Relatively weak vertical shear (no SEC overlying the EUC) and weak meridional shear (SECN and NECC are weak) characterize the flow along 140°W; consistent with weak TIWs at this time of year (Philander 1978; Cox 1980; McCreary and Yu 1992; Donohue and Wimbush 1998; Lyman et al. 2007). The meridional structure of poleward flow in spring/summer (middle panel of Fig. 5) is more symmetric than the annual mean (Mod v in Fig. 1) with northward flow north of the equator only 8 cm/sec faster than the analogous southward flow south of the equator when v_{clim} is averaged over the wind patch (dashed lines indicate the approximate boundaries of the full-amplitude anomalous winds). Equatorial upwelling between 2.5°S and 2.5°N is also weaker than its annual mean (compare lower panel of Fig. 5 and Mod w in Fig. 1), and there is nearly symmetric off-equatorial downwelling (-0.5 m/day at 4.3°S and -0.9 m/day at 3.3°N averaged over the wind patch).

Not surprisingly, in experiments with imposed weakened Trades all elements of the large-scale (zonally low-pass filtered) circulation slow down (Fig. 6). As seen in the 45-day mean of u_L at 5 m (upper panel of Fig. 6), the direct ocean response is an eastward near-surface anomaly. The shoaled EUC is strengthened, both branches of the SEC are weakened off the equator, so the vertical shear between the SEC-EUC and the meridional shear between the SECN-NECC are both decreased. The zonal velocity anomaly propagates eastward as a Kelvin wave and affects the eastern equatorial Pacific from the eastern boundary of the wind patch to the Galapagos Islands. This anomalous Kelvin wave only carries modifications to zonal velocity.

Under the wind patch, the imposed westerly wind anomaly produces anomalous near-surface equatorward flow at 5 m (middle panel of Fig. 6) which reduces the strength of the background tropical circulation cell (middle panel of Fig. 5). This drives anomalous equatorial downwelling and off-equatorial upwelling with maxima between 3° and 4° latitude at 60 m (lower panel of Fig. 6). Although the magnitude of the anomalous velocities are slightly stronger north of the equator, the latitudinal structure of the anomalies is nearly symmetric (for u_L, w_L) or antisymmetric (for v_L) along 140°W.

TIWs are seasonally weak during this time period. Weakening the Trades further decreases the TIW velocity amplitudes and reduces westward propagation speeds by up to 2 cm/sec which adjusts the locations of the TIW crests and troughs (not shown). The reduction of TIW amplitudes is consistent with the reduction of vertical and meridional shears (upper panel of Fig. 6) and the slowdown of TIW propagation is consistent with the weakened SECN (Lyman 2002). During this period, the anomalous TIW variance (short-scale variability removed by low-pass filter in section 2e) north of the equator and east of the wind patch is weak. As a result, the nonlinear rectification on the large-scale anomalous circulation cell by the TIWs is negligible in spring/summer (i.e., (v_L, w_L) are minimally asymmetric under the wind path and near zero east of the wind patch).

2) Fall

During fall, the 45-day mean background circulation is driven by seasonally strong Trades (Fig. 3). The SEC and NECC are both near their annual peaks, with the SEC dominating the surface zonal flow from 10°S to 4.9°N (upper panel of Fig. 7). At this time of year the vertical and meridional shear of u_{clim} is large in the central Pacific consistent with strong background TIWs, predominantly north of the equator. The tropical circulation cell in fall (Fig. 7) is more asymmetric than the annual mean (Mod v, w in Fig. 1) with a band of northward flow north of the equator that is twice as fast as the analogous southward flow south of the equator, and a sharp narrow band of off-equatorial downwelling (-2.3 m/day near 3.5°N averaged over the wind patch). Some of this equatorial asymmetry arises from the linear wind-driven response to the stronger Southeast Trades (Wind (V, w) in Fig. 3). Additional asymmetry can be due to nonlinear advection which includes a large zonal scale contribution (associated with stronger background tropical circulation cell) and a small zonal scale contribution (associated with stronger TIWs), as well as linear processes not included in the equatorially-modified Ekman model.

Because the same anomalous winds are imposed in both seasons, differences between the fall and spring/summer circulation cell anomalies should be due to nonlinearities in the ocean response. Under the wind patch, these differences are due to both the stronger background tropical circulation cell and TIWs. East of the wind patch the anomalous winds are near zero, therefore differences in the circulation cell anomalies in this region are due to TIWs modified by the altered shear carried by the eastward propagating Kelvin wave (section 3a(1)),

As in the spring/summer experiment, weakening the Trades produces an eastward anomaly and reduces the strength of the background tropical circulation cell under the wind patch (Fig. 8). Unlike the earlier case the equatorial asymmetry of v_L and w_L has dramatically increased, with much stronger equatorward flow north of the equator (middle panel of Fig. 8) and a strong narrow band of anomalous upwelling near 4.5°N (lower panel of Fig. 8). In and east of the patch, there is anomalous poleward flow between approximately 2°S and 2°N and equatorward flow near 4°N (middle panel of Fig. 8). The meridional divergence/convergence associated with the complex structure of v_L produces additional upwelling/downwelling anomalies that extend well east of the wind anomaly (lower panel of Fig. 8).

As in spring/summer, weakening the Trades weakens TIW amplitudes, reduces the phase speeds, and shifts the locations of the crests and troughs (not shown). In fall, however, the background TIWs are seasonally strong, and the anomalous TIW velocity fluctuations are up to a factor of four times larger. The anomalous TIW variance is largest north of the equator in and east of the wind patch. This coincides with locations where the fall anomalous circulation cell differs from the spring/summer cell; providing further evidence of nonlinear rectification by TIWs.

b. Vertical structure of the response along 140° *W*

1) Spring/summer

The zonal low-pass filter has removed short zonal scales so the vertical structure of the anomalous response under the wind patch can be described through the 45-day mean along 140°W (Fig. 9). Mean u_L is eastward in the upper 100 m across the waveguide as the anomalous winds weaken the SEC (with stronger modification to the SECN), and increases the strength of the EUC near the surface (upper panel of Fig. 9). Weakening the Trades also reduces the zonal pressure gradient, which weakens the strength of the EUC core by about 8 cm/sec (small westward anomaly at 105 m in Fig. 9). All elements of the tropical circulation cell decrease. The surface limb of the anomalous tropical Pacific circulation cell spans the upper 60 m of the water column. Below 60 m, the anomalous poleward flow is nearly antisymmetric about the equator (second panel of Fig. 9) and counters the background geostrophic convergence (Mod v in Fig. 1). The equatorial downwelling anomaly (maximum at 90 m and at 1°N, 60 m) extends to 200 m (third and fourth panels of Fig. 9) and decreases the strength of the background equatorial upwelling (Mod w in Fig. 1). Nearly symmetric anomalous upwelling with maxima at 3.3°S, 60 m and 3.7°N, 60 m opposes the background off-equatorial downwelling.

2) Fall

In contrast to the spring/summer 45-day mean (u_L, v_L, w_L) along 140°W (Fig. 9), there is significant equatorial asymmetry in the upper 150 m during fall (Fig. 10). Modifications to the anomalous tropical circulation cell are considerably larger north of the equator in fall, with relatively little interseasonal difference south of the equator. There is enhanced asymmetry in v_L with strong near-surface equatorward and subsurface poleward flow north of the equator, tending to reverse the background cell (middle panel of Fig. 10). The sharp divergence of v_L at 4°N drives anomalous off-equatorial upwelling of more than 1 m/day at 70 m depth (third panel of Fig. 10).

c. Geostrophic and ageostrophic response along $140^\circ W$

As the surface limb of the tropical circulation cell is largely contained within the upper 60 m of the water column, the zonally low-pass filtered meridional transport integrated over the upper 60 m (V_L) is used to study the latitudinal structure of the anomalous response along 140°W. This transport is separated into anomalous geostrophic transport (V_G) and ageostrophic transport (V_{AG}) by vertically integrating and filtering geostrophic and ageostrophic currents (section 2). From continuity, w_L at 60 m can be separated into a geostrophic component (w_G) and an ageostrophic component (w_{AG}). In this section, the 45-day mean geostrophic and ageostrophic response in the surface limb of the tropical circulation cell is described, and the meridional and temporal structure of (V_{AG}, w_{AG}) are compared against the meridional structure of the linear equatorially-modified Ekman solutions ((V_τ, w_τ) in Fig. 4) and temporal evolution of the westerly wind anomaly (Fig. 2).

1) Spring/summer

In spring/summer, the relatively large 45-day mean ageostrophic response exceeds the opposing geostrophic response such that (V_L, w_L) spin-down the surface limb of the background circulation cell (upper panels of Fig. 11). The structure of V_{AG} is very similar to V_τ (upper left panel of Fig. 11), except the extrema at 2.3°S and 3.0°N (circles) are larger and slightly asymmetric (ratio of the magnitude of the northern minimum of V_{AG} to that of the southern maximum is 1.08). Similarly w_{AG} compares well with w_τ (upper right panel of Fig. 11) with strong anomalous downwelling along equator between 2.5°S and 2.7°N and nearly symmetric anomalous upwelling with maxima at 3.3°S and 3.7°N. The broad bands of downwelling/upwelling are dominated by the convergence/divergence of meridional transport alone (right panels of Fig. 11). As a result, the off-equatorial extrema of w_{AG} ($\frac{\partial w_{AG}}{\partial y} = 0$) coincide with the inflection points of V_{AG} ($\frac{\partial^2 V_{AG}}{\partial y^2} = 0$) at 3.3°S and 3.7°N (diamonds). The extrema and inflections points will be revisited in section 4b as a means to define the transition from an equatorial to Ekman dynamical response.

Empirical Orthogonal Function (EOF) analysis is used to diagnose the meridional and temporal structure of the spin-down of the tropical circulation cell during the first 31 days of the spring/summer experiment. The latitudinal structures of the first EOF mode of V_{AG} and w_{AG} (Fig. 12) are similar to the structures of (V_τ, w_τ), as well as the 45-day means (Fig. 11). The lower right panel of Fig. 12 compares the first EOF principle component time series with the time evolution of the anomalous winds. Note that the principle component time series by construct have zero time integrals, but have been shifted such that the plotted amplitudes are zero on the first day of the experiment (i.e., the amplitude at $t = 0$ is subtracted from the entire time series). The V_{AG} and w_{AG} time series closely match the time evolution of the westerly wind anomaly with lags of less than a day. This combined with the large fraction of total variance represented by the first EOF of V_{AG} and w_{AG} (94.1% and 66.4%, respectively) provide evidence that the anomalous ageostrophic tropical circulation cell in spring/summer is dominated by a linear equatorially-modified Ekman response.

2) Fall

Although the 45-day mean geostrophic response in fall is similar to the spring/summer response, the mean ageostrophic response is equatorially asymmetric in fall (compare Figs. 11 and 13). South of the equator, V_{AG} is very similar to V_τ (upper left panel of Fig. 13) and the spring/summer experiment (upper left panel of Fig. 11) with maximum and inflection point at 2.3°S and 3.3°S, respectively. North of the equator, however, the magnitude of the northern minimum is much larger than that of the southern maximum (ratio of 1.84), and both the northern minimum and inflection point have shifted poleward to 3.3°N and 4.3°N, respectively. As before, w_{AG} is dominated by $\frac{\partial V_{AG}}{\partial y}$, so the equatorially asymmetry in V_{AG} produces a sharp upwelling peak at 4.3°N that has no counterpart in the south (right panels of Fig. 13).

The latitudinal structures of the first EOF mode of V_{AG} and w_{AG} (Fig. 14) are much like (V_τ, w_τ) and the 45-day means (Fig. 13), however, the anomalous ageostrophic cell is more asymmetric with a sharp peak in w_{AG} near 4°N. This w_{AG} peak narrows and increases in amplitude when EOFs are computed from the full 61 day record (not shown) due to anomalous TIWs which grow in amplitude in the second month of the experiment. The V_{AG} principle component time series closely matches the evolution of the anomalous winds with only a one day lag consistent with a linear equatorially-modified Ekman response. In contrast, w_{AG} lags the anomalous winds by 16 days and is influenced by processes not included in the Ekman balance.

4. Linearity of the Ageostrophic Response

a. First EOF mode

In this section, the linearity of the ageostrophic circulation cell anomalies (V_{AG}, w_{AG}) is analyzed by comparing the EOFs from strengthened Trade winds experiments to those of the weakened Trade winds experiments (section 3c). The strengthened Trades (or easterly wind) anomaly is identical in structure and magnitude to the weakened Trades anomaly (section 2b) differing only in sign. Results from winter experiments are also included to compare the situation as the climatological Trades and TIWs are weakening.

Fig. 15 compares the first mode EOFs for V_{AG} for the strengthened Trades case (blue line) and weakened Trades case (red line) during three different seasons: spring/summer, fall, and winter. Overall, the first mode EOFs represent over 82% of the total variance and the principle component time series are highly correlated with the wind anomaly time series (greater than 0.97 zero-lag correlation). Within a given season, the response of V_{AG} to anomalous winds of opposing sign is nearly identical (e.g., the structures overlap and the time series are mirror-images). The largest differences in the V_{AG} first EOF structures occur between seasons. In particular, there is enhanced equatorial asymmetry and large deviations from the V_τ solution north of the equator in fall and winter.

The response of w_{AG} first EOF mode to anomalous winds of opposing sign is more complex (Fig. 16). In spring/summer, the structures for strengthened and weakened winds are nearly identical and represent a large fraction of the total variance (about 67%), and the time series are highly correlated with the wind anomaly time series (approximately 0.97 zero-lag correlation; upper panels of

Fig. 16). By contrast, fall and winter responses show upwelling and downwelling peaks with very small meridional scales that do not overlap for the strengthened and weakened Trades. The fraction of variance represented by the first mode (between 55% and 65%) and the correlations with the wind anomaly time series (0.35 to 0.8) are also significantly smaller for these seasons. Given that the magnitude and structure of the wind anomalies are the same for all these experiments, Figs. 15 and 16 effectively demonstrate that the anomalous circulation cell is dominated by the linear equatorially-modified Ekman response in spring/summer, but nonlinear processes play a major role in fall and winter.

b. Zonal wind experiment statistics

Little is known from observations about the latitude at which the tropical circulation cell transitions from its equatorial structure to an Ekman-like structure. Here, the transition is defined by both the extrema of V_{AG} where the curve ceases growing with decreasing latitude, and by the off-equatorial inflection points of V_{AG} where the off-equatorial extrema of w_{AG} are found (section 3c). For the linear equatorially-modified Ekman model with $r_s^{-1} = 2$ day, these occur at 2.3° and 4° latitude, respectively, in both hemispheres (section 2d). Table 2 compiles the locations of the 45-day mean V_{AG} extrema and inflection points as well as the ratio of the magnitude of the northern extremum to southern extremum for the weakened and strengthened Trades runs. These statistics are a convenient measure to quantify the deviations of V_{AG} from the linear antisymmetric V_τ. To further the linearity analysis, results from one-tenth magnitude versions of the weakened and strengthened Trades runs are also included.

In general, the structure of V_{AG} depends more on the season than the sign and magnitude of imposed zonal wind anomaly (Table 2). During spring/summer, the ratio of the extrema magnitudes is close to unity (i.e., antisymmetry) with average value of 1.08 and the extrema and inflection points are relatively close to the equator. During fall and winter, on the other hand, the equatorial asymmetry is much larger. The extrema and inflection points shift poleward by 0.1° to 1.6° (more pronounced north of the equator) and the ratio of the extrema has increased (1.36 ± 0.16 and 1.61 ± 0.16 in the winter and fall, respectively). Note for all seasons the distance between extrema and inflection points is less than the 1.7° predicted by equatorially-modified Ekman model with $r_s^{-1} = 2$ day (section 2d).

By manipulating (6) and (7) in section 2d and substituting the 45-day mean V_{AG} and w_{AG} in place of V_τ and w_τ, estimates of r_s^{-1} can be obtained from the model. Using w_{AG} at the equator in (7) gives

$$r_s^{-1} = \sqrt{\frac{-\rho w_{AG}(y = 0°)}{\beta \tau_x(y = 0°)}}. \tag{8}$$

Using the latitude and magnitude of V_{AG} extrema in (6) gives

$$r_s^{-1} = (\beta |y_{ext}|)^{-1} \tag{9}$$

$$r_s^{-1} = \frac{2\rho |V_{AG}(y = y_{ext})|}{|\tau_x(y = y_{ext})|}. \tag{10}$$

Table 3 compares the values of r_s^{-1} obtained from (8)-(10). Overall, $r_s^{-1} = 2$ day was a suitable choice for the zonal wind experiments conducted here. This is especially true in spring/summer or when r_s^{-1} is estimated from the equatorial value of w_{AG} or the southern extremum of V_{AG} (r_s^{-1} between 1.7 and 2.8 day). In the fall and winter, widely differing values are estimated for r_s^{-1} from the location (r_s^{-1} as small as 1.3 day) and magnitude (r_s^{-1} as large as 3.8 day) of the northern extremum reflecting how much the ageostrophic anomalies deviate from the equatorially-modified Ekman solution during those time periods.

5. Summary and Conclusions

The zonal currents in the central equatorial Pacific are strong, and robust estimates have been made of their strength, spatial structure, and temporal evolution. Much less is known about the meridional-upwelling circulation cell, as we have only sparse measurements of the upper-ocean meridional and vertical velocities and these are often aliased by TIWs. Yet, vertical and meridional heat fluxes have been shown to be more important than zonal heat flux for sustaining the equatorial Pacific cold tongue and its sharp temperature gradients (e.g., Swenson and Hansen 1999). Therefore, better sampling is required of the full three-dimensional circulation across the cold tongue, and this sampling must resolve TIW fluctuations which also contribute significantly to the heat flux balance (Hansen and Paul 1984; Bryden and Brady 1989; Baturin and Niiler 1997; Wang and McPhaden 1999; Swenson and Hansen 1999; Wang and McPhaden 2000). In anticipation of these measurements, here we have conducted perturbed Trade winds experiments in an OGCM, to study the three-dimensional structure of the velocities in the central equatorial Pacific and the mechanisms by which the tropical circulation cell responds to wind variations. Findings from this numerical study will aid in the design of future field experiments with the goal of resolving, and adequately sampling, the spatio-temporal structure of the tropical circulation cell.

To analyze the spin-down of the tropical circulation cell along 140°W in response to the localized weakening of the Trade Winds, a series of experiments were conducted which add a westerly wind anomaly to the climatological wind stress. To diagnose the role of the background currents and TIWs, the 61-day experiments were repeated during three different phases of the annual cycle: boreal spring/summer, fall, and winter. Emphasis was placed on the spring/summer and fall cases which represent extremes of the annual evolution of the Trades (Fig. 3) and TIWs. Equatorially-modified versions of geostrophy and Ekman theory and zonal low-pass filtering were used to isolate the mechanisms of the large zonal scale wind-driven response. The near-surface linear response to the imposed weakened Trades anomaly is equatorially symmetric eastward transport, equatorial downwelling, antisymmetric equatorward transport with maxima at 2.3° latitude, and symmetric off-equatorial upwelling with maxima at 4.0° latitude (Fig. 4).

Weakening the Trades in any season rapidly weakened the tropical circulation cell (Figs. 6 and 8). The zonal current shear was also reduced which had the effect of reducing the amplitude and propagation speed of TIWs in and east of the wind patch. In spring/summer when the background Southeast Trades, zonal currents, and TIWs were seasonally weak, the large zonal scale response of the circulation was nearly linear (e.g., equatorially symmetric in u_L, w_L and antisymmetric in v_L). In fall when the background winds and TIWs were seasonally strong, the anomalous circulation under the wind patch was equatorially asymmetric with a strong narrow band of anomalous upwelling produced north of the equator. The fall experiments showed clear evidence of nonlinear rectification by the modified TIWs onto the circulation cell north of the equator and east of the wind patch. This rectification likely also occurred under the wind patch itself, but was difficult to separate from the large nonlinear interactions with the seasonally strong background flow.

Along 140°W, the linear equatorially-modified Ekman solutions largely explained the anomalous ageostrophic response of the tropical circulation cell. In spring/summer, the meridional structure of the means and first mode EOFs of (V_{AG}, w_{AG}) were very similar to those of (V_τ, w_τ) and the temporal evolution of the principle component time series matched the time evolution of the anomalous winds with lags of less than a day. In fall, however, equatorial asymmetry in V_{AG} produced a sharp off-equatorial peak in w_{AG} near 4°N which intensified as the anomalous TIWs grew in amplitude. Within a given season, the ageostrophic responses in the tropical circulation cell were essentially linear, and applying an anomaly of opposite sign produced a nearly identical cell structure with mirror-image time series. The largest differences in the circulation cell structure occurred between seasons and the most significant nonlinearities were found for w_{AG} in fall and winter.

The extrema and inflection points of the near-surface V_{AG} were used to define the transition from an equatorial to Ekman dynamical response. Based on the dominant contribution of $\frac{\partial V_{AG}}{\partial y}$ to w_{AG}, the inflection points of V_{AG} correspond to off-equatorial extrema of w_{AG}. During the spring/summer weak wind season, the extrema and inflections points were relatively close to the equator and $r_s^{-1} = 2$ day was a suitable choice for the zonal wind experiments. In fall/winter, the extrema and inflection points were shifted poleward by up to 1.6°, and widely differing values were estimated for r_s^{-1} from the location and magnitude of the northern extremum (ranging from 1.3 day to 3.8 day).

The source of these interseasonal differences are nonlinear interactions with the background tropical circulation cell and nonlinear rectification by the TIWs. Quantification of the relative contributions of the two hypothesized sources of nonlinearity is needed to understand the equatorial asymmetry of the tropical circulation cell in the central equatorial Pacific. How little is known about these nonlinear interactions points to the need for cross-equatorial velocity measurements that can resolve the influence of TIWs on the tropical circulation cell under varying winds. Based on the substantial contribution of $\frac{\partial V}{\partial y}$ to w in the model, the broad off-equatorial downwelling in spring/summer can be measured from synoptic measurements of meridional velocity with relatively coarse meridional sampling (as long as there is adequate temporal resolution to filter out the seasonally weak TIWs). In contrast, fine meridional sampling (on the order of 0.5°) and sampling along adjacent meridians are required in fall and winter to determine whether the sharp narrow band of downwelling near 4°N results from rectification by TIWs.

Appendix A. Details of Geostrophic Adjustment

a. u_g adjustment

To compute u_g near the equator along a meridian x_0, the Picaut and Tournier (1991) adjustment to the dynamic heights can be written as

$$\widehat{\Phi}(x_0, y) = \Phi(x_0, y) + \Phi'(x_0, y) \qquad \text{(A1)}$$

$$\text{where } \Phi'(x_0, y) = -\Phi_y(x_0, 0) y e^{-y^2/L^2} \qquad \text{(A2)}$$

and the decay length scale has been chosen to be $L = 2^\circ$. This adjustment ensures continuity of u_g across the equator and preserves its non-singular solution at the equator (section 2c). This can be seen from the first and second meridional derivatives of $\widehat{\Phi}(x_0, y)$

$$\widehat{\Phi}_y(x_0, y) = \Phi_y(x_0, y) - \Phi_y(x_0, 0)\left(1 - \frac{2y^2}{L^2}\right)e^{-y^2/L^2} \qquad \text{(A3)}$$

$$\widehat{\Phi}_{yy}(x_0, y) = \Phi_{yy}(x_0, y) - \Phi_y(x_0, 0)\left(\frac{2y}{L^2}\right)\left(\frac{2y^2}{L^2} - 3\right)e^{-y^2/L^2}. \qquad \text{(A4)}$$

Note that $\widehat{\Phi}_y(x_0, 0) = 0$ and $\widehat{\Phi}_{yy}(x_0, 0) = \Phi_{yy}(x_0, 0)$.

b. u_g and v_g adjustment

To estimate both u_g and v_g near the equator, dynamic heights along the meridians x_0 and $x_0 \pm \Delta x$ are modified by an additional adjustment term that affects only the x-derivative

$$\widehat{\Phi}(x, y) = \Phi(x, y) + \Phi'(x_0, y) + \Phi''(x, y) \qquad \text{(A5)}$$

$$\text{where } \Phi''(x, y) = -\Phi_x(x_0, 0)(x - x_0)e^{-y^2/L^2}. \qquad \text{(A6)}$$

Note $\Phi'(x_0, y)$ is still given by (A2) and $L = 2°$ for both adjustment terms. The $\Phi''(x, y)$ term ensures the continuity of v_g across the equator and preserves its non-singular solution at the equator (section 2c). This can be seen from the x and xy derivatives of $\widehat{\Phi}(x, y)$. The correction $\Phi'(x_0, y)$ does not depend on x and therefore the x-derivatives have the form

$$\widehat{\Phi}_x(x, y) = \Phi_x(x, y) - \Phi_x(x_0, 0)e^{-y^2/L^2}, \qquad \text{(A7)}$$

which reduces to zero at the equator, and

$$\widehat{\Phi}_{xy}(x, y) = \Phi_{xy}(x, y) + \Phi_x(x_0, 0)\left(\frac{2y}{L^2}\right)e^{-y^2/L^2} \qquad \text{(A8)}$$

which reduces to $\Phi_{xy}(x, 0)$ at the equator. The Picaut and Tournier (1991) u_g adjustment given by equations (A3)-(A4) is also preserved as $\Phi''(x, y)$ vanishes when $x = x_0$. Continuous zonal and meridional geostrophic velocities along $x = x_0$ can then be computed using (A3) and (A7) away from the equator and (A4) and (A8) at the equator (section 2c).

6. Acknowledgments

The authors would like to thank Andrew Wittenberg, Stephen Griffies, and MOM4 modeling community for helpful discussions about the model viscosity scheme and its impact on the model TIWs. Special thanks to Andrew Wittenberg for running the climatological spin-up on the NOAA/GFDL supercomputer. Meghan Cronin and Dennis Moore helped interpret the transient signals present in the anomalous response. The authors also thank Craig Risien, Dudley Chelton, and Michael Schlax for providing an early version of the QuikSCAT climatology. The authors were funded by NOAA/CPO and this research was performed while RCP held a NRC Research Associateship Award at NOAA/PMEL.

7. References

Baturin, N. G., and P. P. Niiler, 1997: Effects of instability waves in the mixed layer of the equatorial Pacific, *J. Geophys. Res.*, **102**, 27,771-27,793.

Bonjean, F., and G. S. E. Lagerloef, 2002: Diagnostic model of the surface currents in the tropical Pacific Ocean. *J. Phys. Oceanogr.,* **32**, 2938-2954.

Bryden, H., and E. C. Brady, 1989: Eddy momentum and heat fluxes and their effects on the circulation of the equatorial Pacific Ocean. *J. Mar. Res.,* **47,** 55-79.

Chelton, D. B., and Coauthors, 2001: Observations of coupling between surface wind stress and sea surface temperature in the eastern tropical Pacific. *J. Climate*, **14**, 1479-1498.

Contreras, R. F., 2002: Long-term observations of tropical instability waves. *J. Phys. Oceanogr.,* **32**, 2715-2722.

Cox, M. D., 1980: Generation and propagation of 30-day waves in a numerical model of the Pacific. *J. Phys. Oceanogr.,* **10,** 1168-1186.

Donohue, K. A., and M. Wimbush, 1998: Model results of flow instabilities in the tropical Pacific Ocean. *J. Geophys. Res.,* **103**, 21,401-21,412.

Griffies, S. M., M. J. Harrison, R. C. Pacanowski, and A. Rosati, 2003: A technical guide to MOM4. GFDL Ocean Group Tech. Rep. 5, NOAA/Geophysical Fluid Dynamics Laboratory, Princeton, NJ, 295 pp.

Griffies, S. M., A. Gnanadesikan, K. W. Dixon, J. P. Dunne, R. Gerdes, M. J. Harrison, A. Rosati, J. L. Russell, B. L. Samuels, M. J. Spelman, M. Winton, and R. Zhang, 2005: Formulation of an ocean model for global climate simulations. *Ocean Sci.*, **1**, 45-79.

Hansen, D. V., and C. A. Paul, 1984: Genesis and effects of long waves in the equatorial Pacific. *J. Geophys. Res.,* **89,** 10 431-10 440.

Hayes, S. P, Mangum, L. J., Picaut, J., Sumi, A., Takeuchi, K., 1991: TOGA-TAO: a moored array for real-time measurements in the tropical Pacific Ocean. *Bulletin of the American Meteorological Association*, **72**, 339-347.

Johnson, E. S., and D. S. Luther, 1994: Mean zonal momentum balance in the upper and central equatorial Pacific ocean. *J. Geophys. Res.,* **99**, 7689-7705.

Johnson, G. C., M. J. McPhaden, and E. Firing, 2001: Equatorial Pacific ocean horizontal velocity, divergence, and upwelling. *J. Phys. Oceanogr.,* **31**, 839-849.

Johnson, G. C., B. M. Sloyan, W. S. Kessler, and K. E. McTaggart, 2002: Direct measurements of upper ocean currents and water properties across the tropical Pacific Ocean during the 1990s. *Progress in Oceanography*, Vol. 52, Pergamon, 31-61.

Kennan, S. C., and P. J. Flament, 2000: Observations of a tropical instability vortex. *J. Phys. Oceanogr.,* **30**, 2277-2301.

Kessler, W. S., and B. A. Taft, 1987: Dynamic heights and zonal geostrophic transports in the central tropical Pacific during 1979-84. *J. Phys. Oceanogr.,* **17**, 97-122.

Kessler, W. S., L. M. Rothstein, and D. Chen, 1998: The annual cycle of SST in the eastern tropical Pacific, diagnosed in an ocean GCM. *J. Climate*, **11**, 777-799.

Kroger, J., A. J. Busalacchi, J. Ballabrera-Poy, and P. Malanotte-Rizzoli, 2005: Decadal variability of shallow cells and equatorial sea surface temperature in a numerical model of the Atlantic. *J. Geophys. Res.,* **110**, C12003, doi:10.1029/2004JC002703.

Lagerloef, G. S. E., G. T. Mitchum, R. B. Lukas, P. P. Niiler, 1999: Tropical Pacific near-surface currents estimated from altimeter, wind, and drifter data. *J. Geophys. Res.,* **104**, 23313-23326.

Large, W. G., G. Danabasoglu, J. C. McWilliams, P. R. Gent, and F. O. Bryan, 2001: Equatorial circulation of a global ocean climate model with anisotropic horizontal viscosity. *J. Phys. Oceanogr.,* **31**, 518-536.

Legeckis, R., 1977: Long waves in the equatorial Pacific Ocean: A view from a geostationary satellite. *Science*, **197**, 1179-1181.

Lyman, J. M., 2002: The cross-equatorial structure of tropical instability waves in sea surface height. Ph.D. thesis, Oregon State University, 134 pp.

Lyman, J. M., G. C. Johnson, and W. S. Kessler, 2007: Distinct 17- and 33-day tropical instability waves in subsurface observations. *J. Phys. Oceanogr.,* **37**, 855-872.

McCreary, J. P., and Z. Yu, 1992: Equatorial dynamics in a 2.5-layer model. *Prog. Oceanogr.*, **29**, 61-132.

McPhaden, M. J., 1993: TOGA-TAO and the 1991-1993 El Niño Southern Oscillation event. *Oceanogr.*, **6**, 36-44.

Nonaka, M., S.-P. Xie, and J. P. McCreary, 2002: Decadal variations in the subtropical cells and equatorial Pacific SST. *Geophys. Res. Lett.*, **29**, 1117, doi:10.1029/2001GL013676.

Philander, S. G. H., 1978: Instabilities of zonal equatorial currents, Part 2. *J. Geophys. Res.,* **83**, 3679-3682.

Picaut, J., and R. Tournier, 1991: Monitoring the 1979-1985 equatorial Pacific current transports with expendable bathythermograph data. *J. Geophys. Res.,* **96**, 3263-3277.

Qiao, L., and R. H. Weisberg, 1995: Tropical instability wave kinematics: Observations from the Tropical Instability Wave Experiment. *J. Geophys. Res.,* **100**, 8677-8693.

Reverdin, G., C. Frankignoul, E. Kestenare, and M. J. McPhaden, 1994: Seasonal variability in the surface currents of the equatorial Pacific. *J. Geophys. Res.,* **99**, 20323-20344.

Risien, C. M., and D. B. Chelton, 2008: A global climatology of surface wind and wind stress fields from 8 years of QuikSCAT scatterometer data. *Resubmitted to J. Phys. Oceanogr.*

Schlax, M. G., and D. B. Chelton, 1992: Frequency domain diagnostics for linear smoothers. *J. Amer. Stat. Assoc.*, **87**, 1070-1081.

Seo, H., M. Jochum, R. Murtugudde, A. J. Miller, and J. O. Roads, 2007: Feedback of tropical instability wave - induced atmospheric variability onto the ocean. *Submitted to J. Climate.*

Steele, M., R. Morley, and W. Ermold, 2001: PHC: A global ocean hydrography with a high-quality Arctic Ocean. *J. Climate*, **14**, 2079-2087.

Swenson, M. S., and D. V. Hansen, 1999: Tropical Pacific Ocean mixed layer heat budget: The Pacific cold tongue. *J. Phys. Oceanogr.,* **29,** 69-81.

Wang, W., and M. J. McPhaden, 1999: The surface-layer heat balance in the equatorial Pacific Ocean. Part I: The mean seasonal cycle. *J. Phys. Oceanogr.,* **29,** 1812-1831.

Wang, W., and M. J.McPhaden, 2000: The surface-layer heat balance in the equatorial Pacific Ocean. Part II: Interannual variability. *J. Phys. Oceanogr.,* **30,** 2989-3008.

Weisberg, R. H., and L. Qiao, 2000: Equatorial upwelling in the central Pacific estimated from moored velocity profilers. *J. Phys. Oceanogr.,* **30**, 105-124.

Wittenberg, A. T., 2002: ENSO response to altered climated. Ph.D. thesis, Princeton University, 475 pp.

Wittenberg, A. T., A. Rosati, N.-C. Lau, and J. J. Ploshay, 2006: GFDL's CM2 global coupled climate models. Part III: Tropical Pacific climate and ENSO. *J. Climate*, **19**, 698-722.

Wyrtki, K., 1981: An estimate of equatorial upwelling in the Pacific. *J. Phys. Oceanogr.,* **11**, 1205-1214.

Yu, L., and R. A. Weller, 2007: Objectively analyzed air-sea heat fluxes for the global ice-free oceans (1981-2005). *Bull. Ameri. Meteor. Soc.*, **88**, 527-539.

Yu, L., R. A. Weller, and B. Sun, 2004: Improving latent and sensible heat flux estimates for the Atlantic Ocean (1988-99) by a synthesis approach. *J. Climate*, **17**, 373-393.

Zhang, Y., W. B. Rossow, A. A. Lacis, V. Oinas, and M. I. Mishchenko, 2004: Calculation of radiative fluxes from the surface to top of atmosphere based on ISCCP and other global data sets: Refinements of the radiative transfer model and the input data. *J. Geophys. Res.,* **109**, D19105, doi:10.1029/2003JD004457.

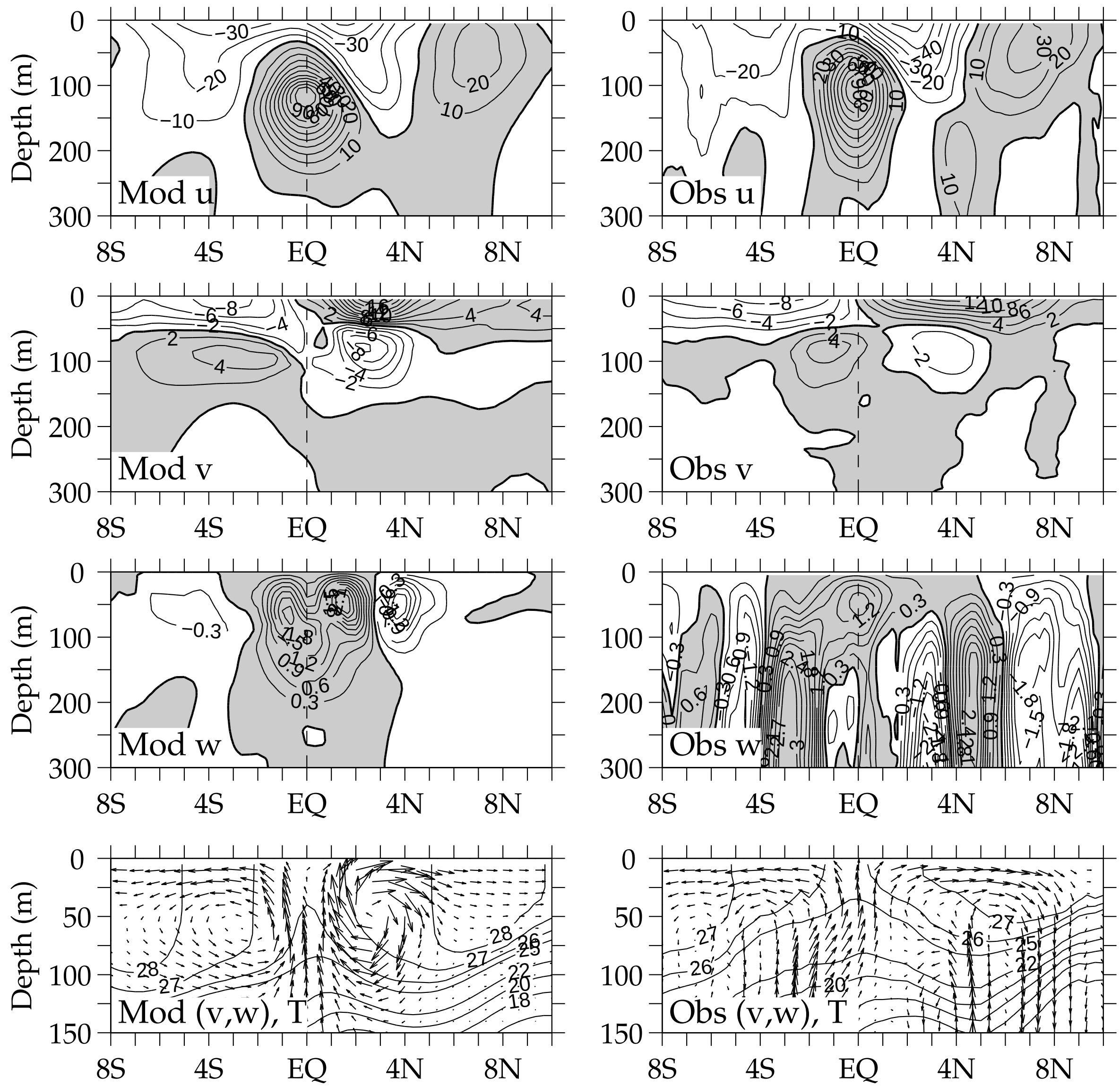

Figure 1. Mean circulation along 140°W from MOM4 simulation driven by climatological forcing compared with mean circulation along 136°W estimated from 85 meridional ADCP transects (reproduced from Johnson et al. 2001). Contour intervals for mean u, v, and w are 10 cm/sec, 2 cm/sec, and 0.3 m/day, respectively. Thick solid line corresponds to zero contour and shaded contours indicate positive values. Scaled vectors depict the tropical circulation cell in the upper 150 m with select mean temperature contours overlaid.

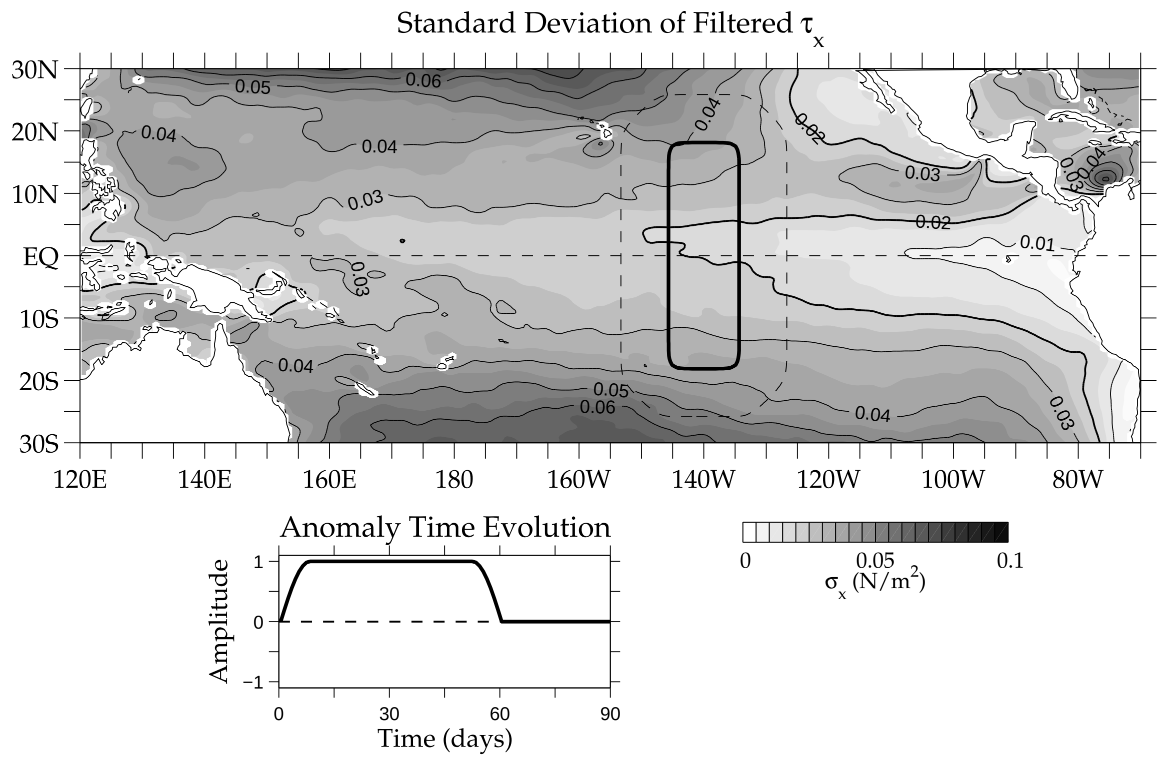

Figure 2. Standard deviation of QuikSCAT zonal windstress on intra-annual timescales in N m^{-2} in the upper panel. Annual cycle removed and 400-day high-pass triangle filter applied to remove annual and interannual variability. Solid box indicates region where anomalous winds approximately equals A and dashed box indicates region where anomalous winds have tapered to zero. The temporal evolution of zonal wind anomaly is plotted in the lower panel.

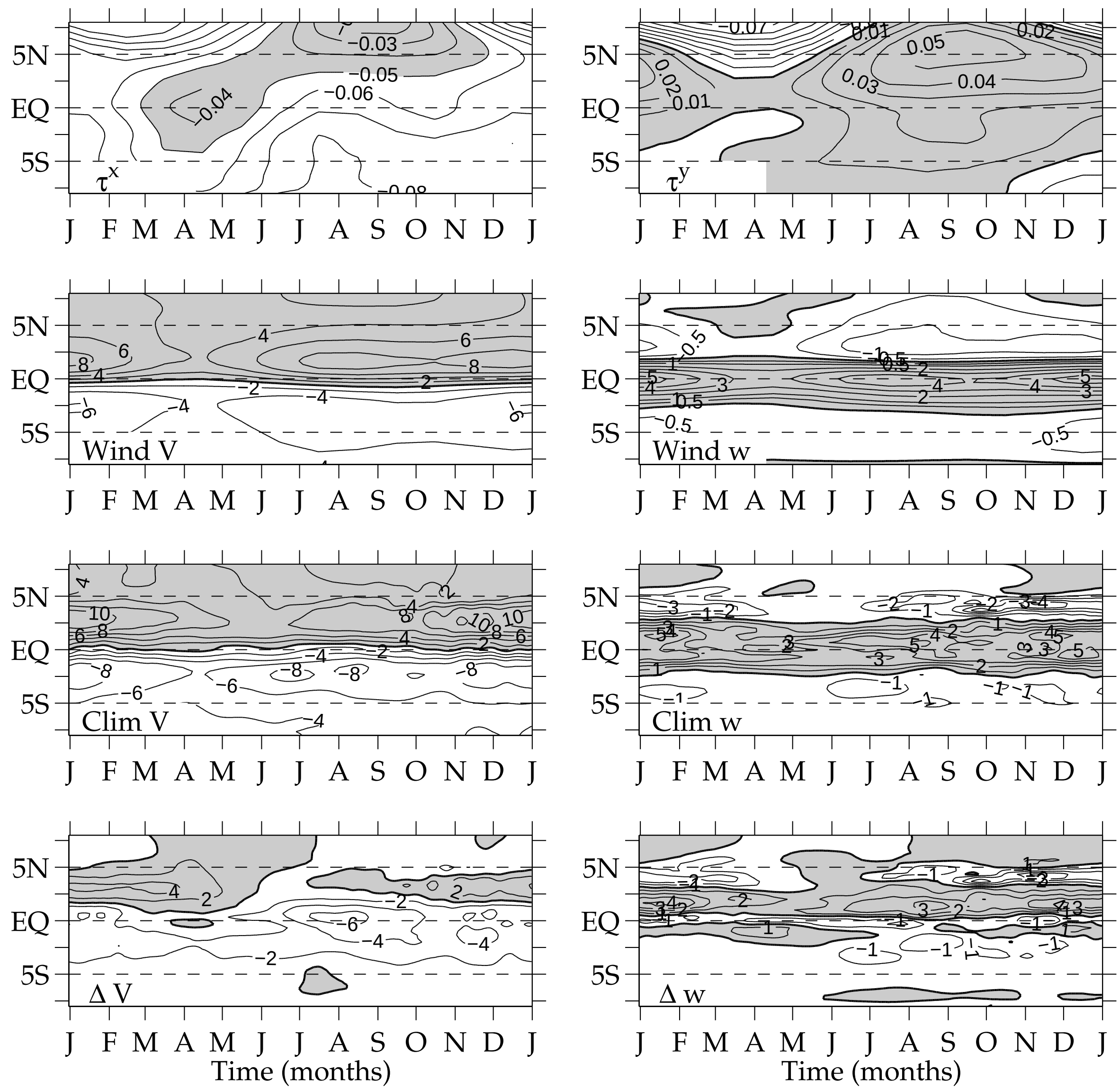

Figure 3. QuikSCAT windstress climatology (τ_x, τ_y), equatorially-modified Ekman meridional transport and vertical velocity (Wind V, w), 60-day low-pass filtered ageostrophic meridional transport and vertical velocity from control run (Clim V, w), and difference between ageostrophic and equatorially-modified Ekman values $(\Delta V, \Delta w)$ along 140°W as a function of time. Contour intervals for windstress, transport, and vertical velocity are 0.01 N m^{-2}, 2 m^2/sec, and 1 m/day (with addition of ± 0.5 m/day contour for Wind w), respectively. Thick solid line corresponds to zero contour and shaded contours indicate positive values (except for τ_x where weak easterlies are shaded).

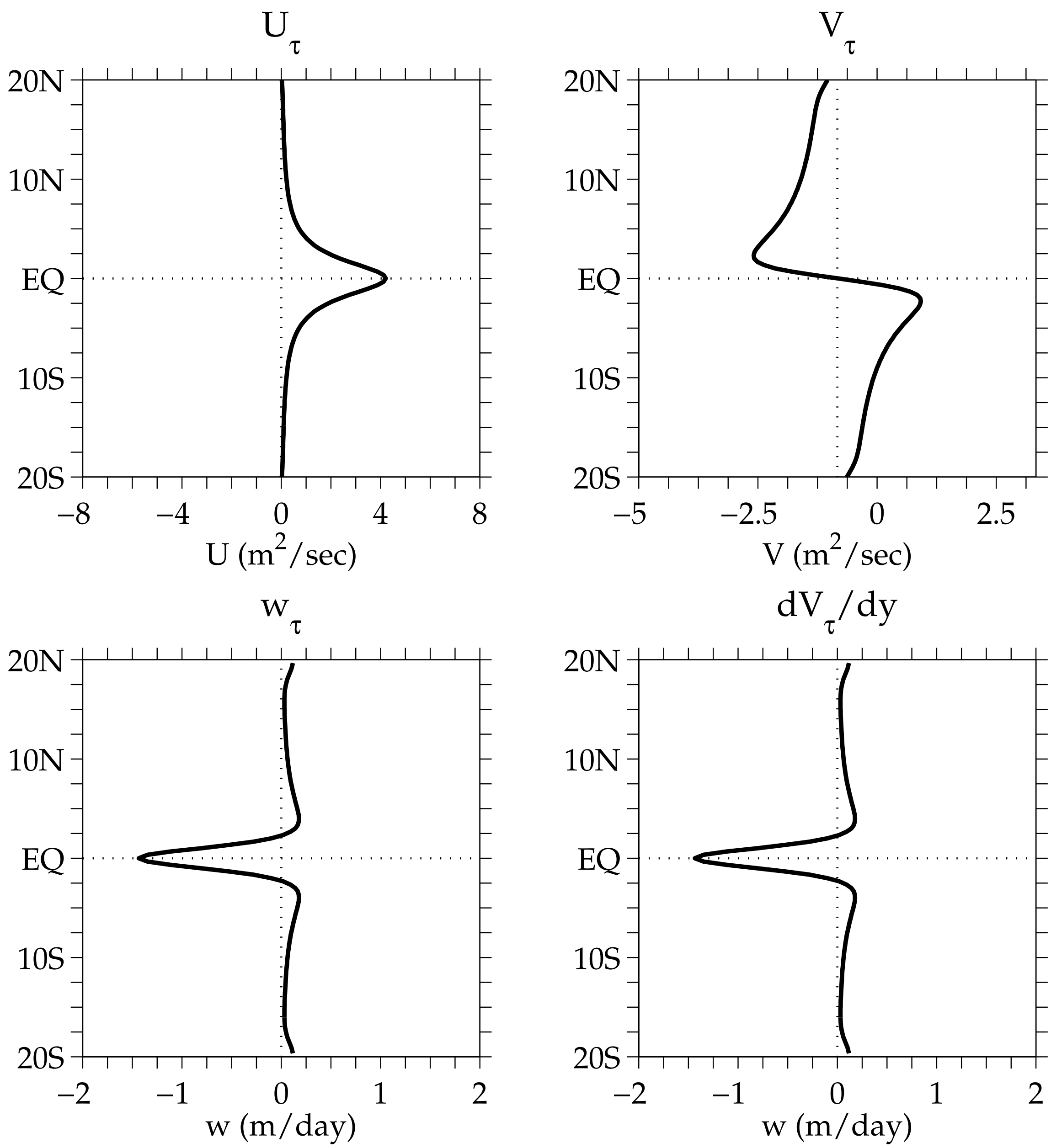

Figure 4. Equatorially-modified Ekman zonal (upper left panel) and meridional (upper right panel) transport for weakened zonal Trade wind anomaly. Ekman vertical velocity computed from the depth-integrated continuity equation using full transport (lower left panel) and meridional transport (lower right panel).

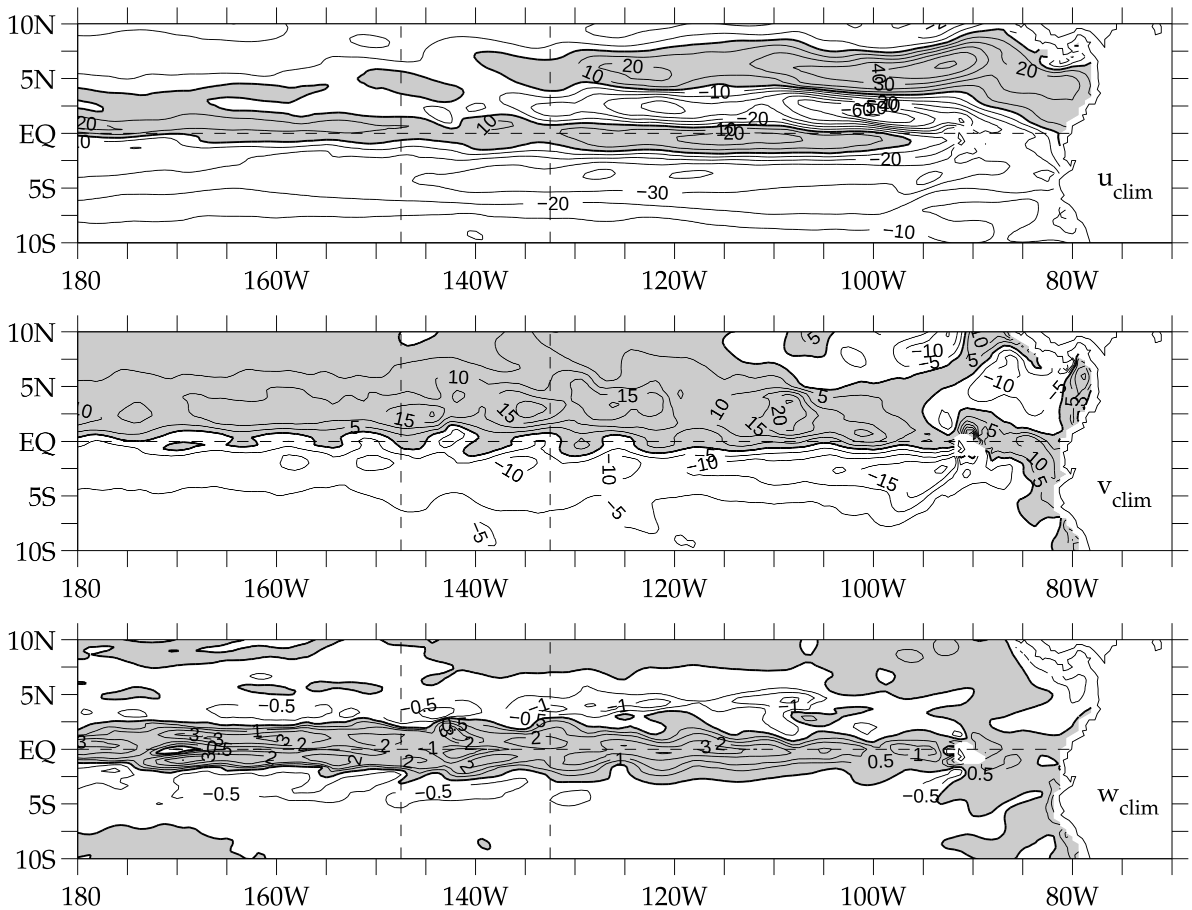

Figure 5. 45-day mean surface circulation from climatological control run during spring/summer. Horizontal velocity shown at 5 m depth and vertical velocity at 60 m depth. Contour intervals for mean u_{clim}, v_{clim}, and w_{clim} are 10 cm/sec, 5 cm/sec, and 1 m/day (with addition of ± 0.5 m/day contour), respectively. Thick solid line corresponds to zero contour and shaded contours indicate positive values.

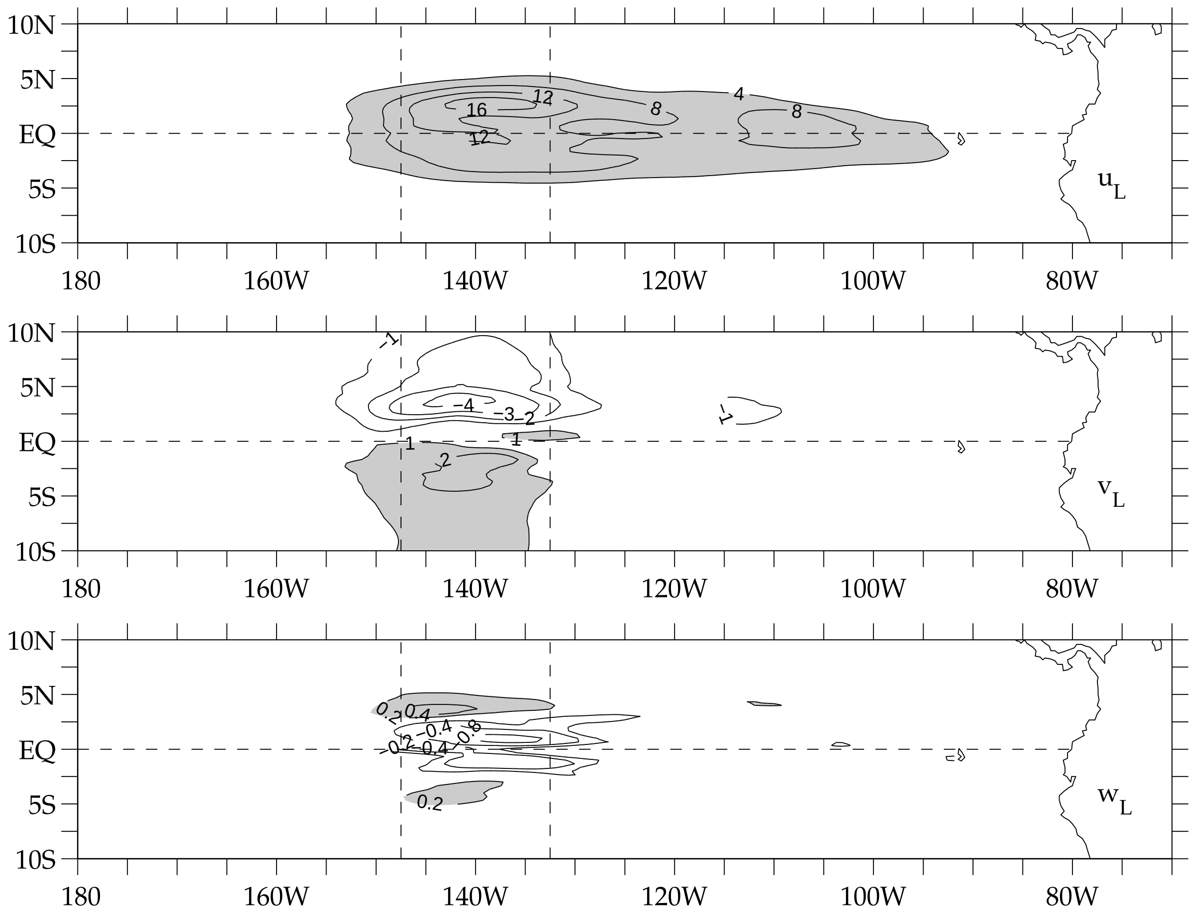

Figure 6. 45-day mean zonally low-pass filtered surface circulation from weakened Trades run minus the control circulation during spring/summer. Horizontal velocity shown at 5 m depth and vertical velocity at 60 m depth. Contour intervals for mean u_L, v_L, and w_L are 4 cm/sec, 1 cm/sec, and 0.4 m/day (with addition of ± 0.2 m/day contour), respectively. Shaded contours indicate positive values. The zero contour is not plotted.

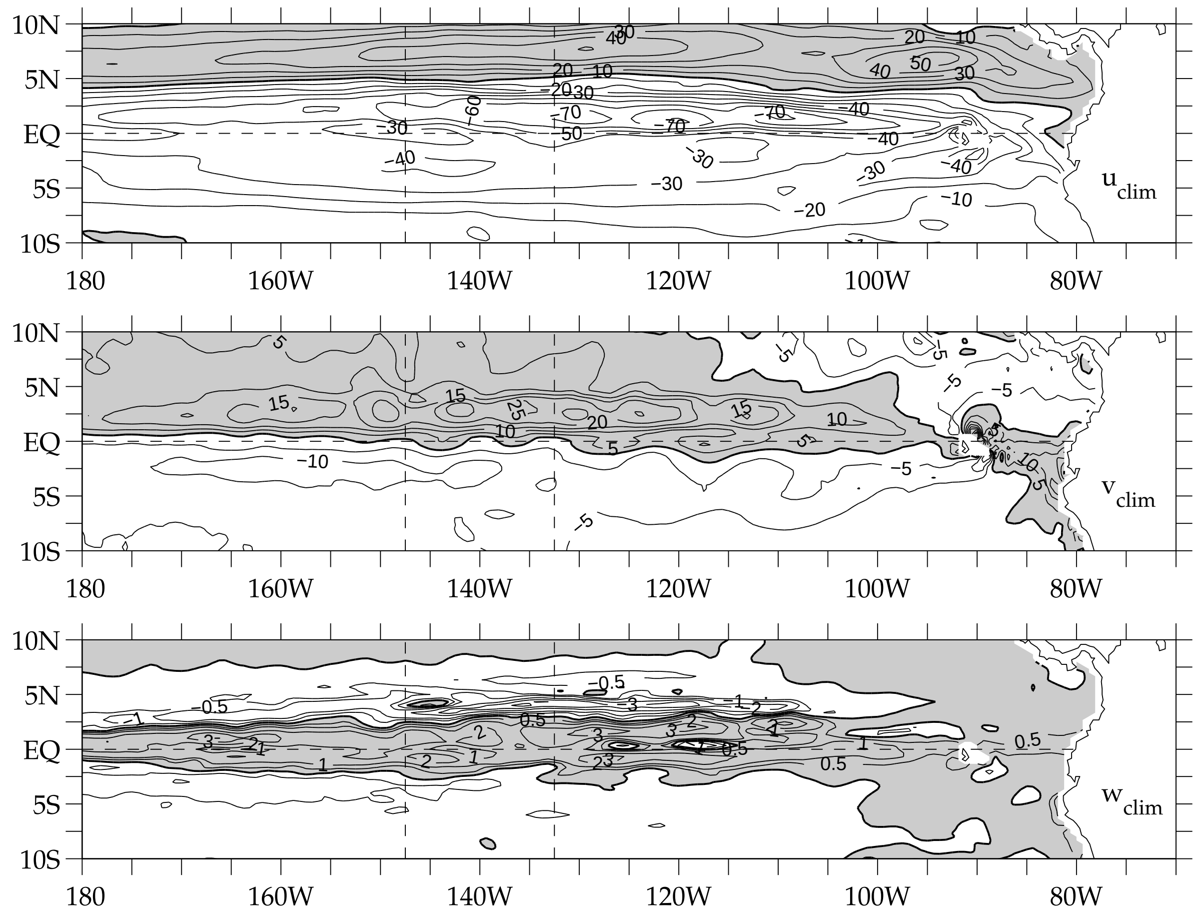

Figure 7. 45-day mean surface circulation from climatological control run during fall. Horizontal velocity shown at 5 m depth and vertical velocity at 60 m depth. Contour intervals for mean u_{clim}, v_{clim}, and w_{clim} are 10 cm/sec, 5 cm/sec, and 1 m/day (with addition of ± 0.5 m/day contour), respectively. Thick solid line corresponds to zero contour and shaded contours indicate positive values.

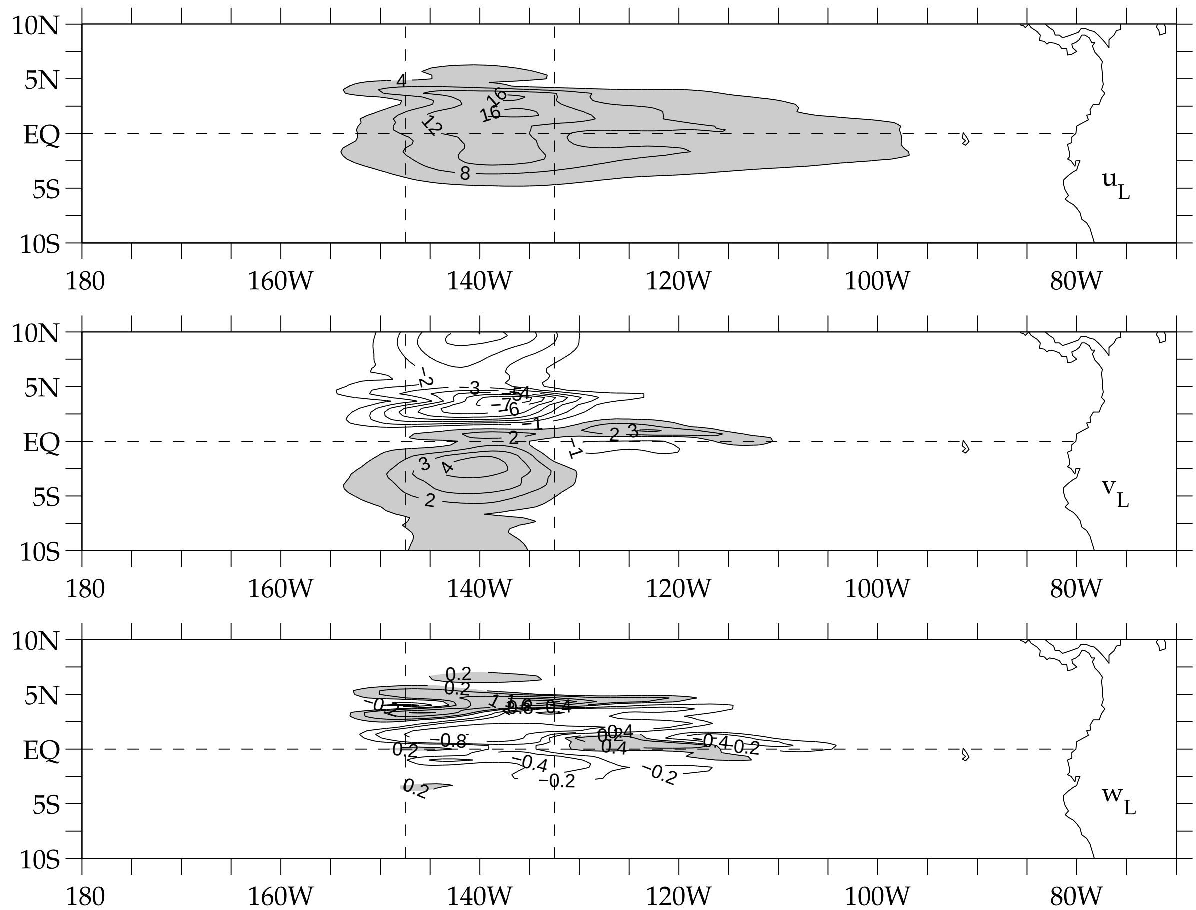

Figure 8. 45-day mean zonally low-pass filtered surface circulation from weakened Trades run minus the control circulation during fall. Horizontal velocity shown at 5 m depth and vertical velocity at 60 m depth. Contour intervals for mean u_L, v_L, and w_L are 4 cm/sec, 1 cm/sec, and 0.4 m/day (with addition of ± 0.2 m/day contour), respectively. Shaded contours indicate positive values. The zero contour is not plotted.

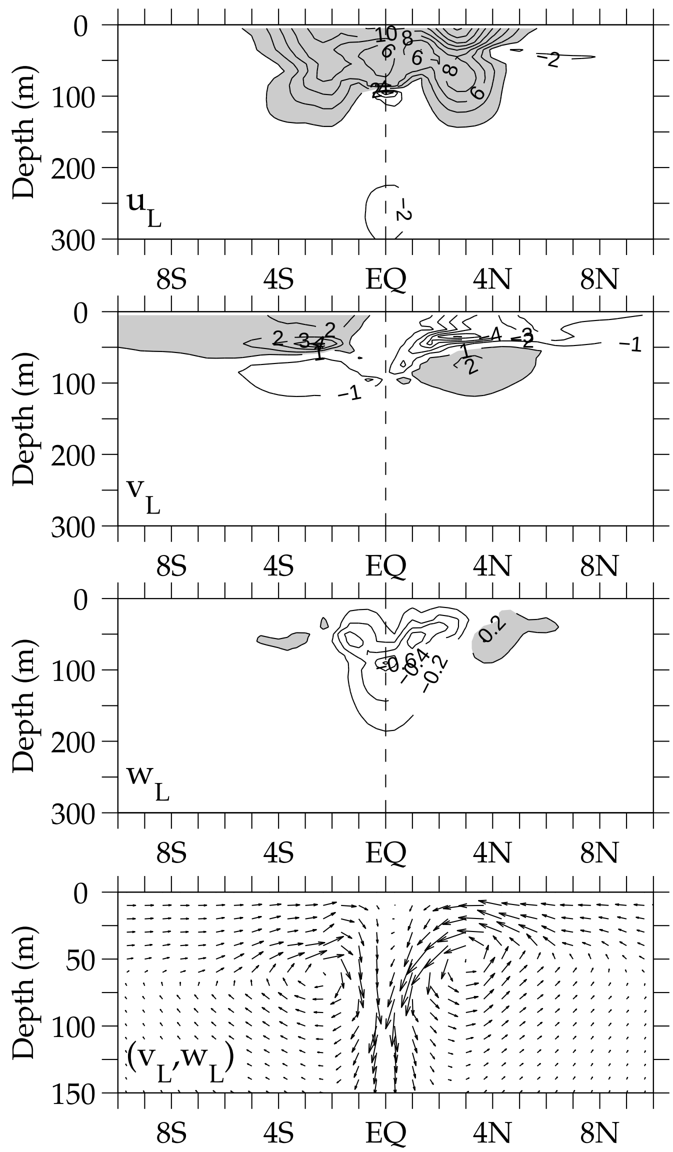

Figure 9. 45-day mean zonally low-pass filtered circulation along 140°W from weakened Trades run minus the control circulation during spring/summer. Contour intervals for mean u_L, v_L, and w_L are 2 cm/sec, 1 cm/sec, and 0.2 m/day, respectively. Shaded contours indicate positive values. The zero contour is not plotted. Scaled vectors depict the anomalous tropical circulation cell in the upper 150 m.

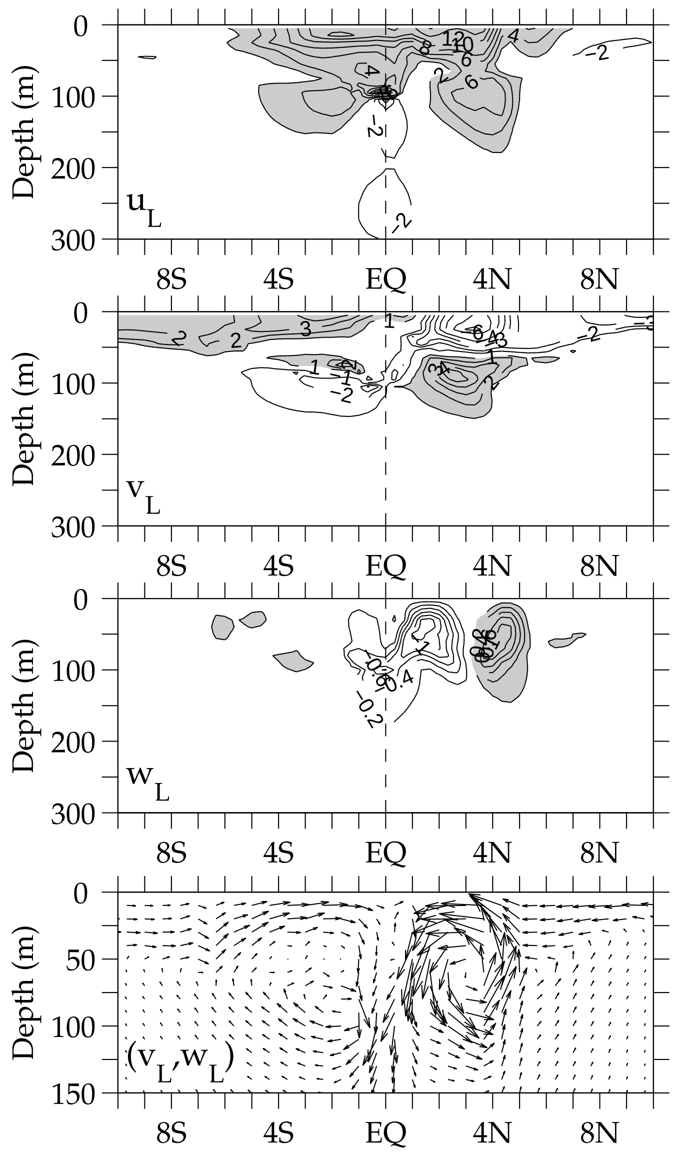

Figure 10. 45-day mean zonally low-pass filtered circulation along 140°W from weakened Trades run minus the control circulation during fall. Contour intervals for mean u_L, v_L, and w_L are 2 cm/sec, 1 cm/sec, and 0.2 m/day, respectively. Shaded contours indicate positive values. The zero contour is not plotted. Scaled vectors depict the anomalous tropical circulation cell in the upper 150 m.

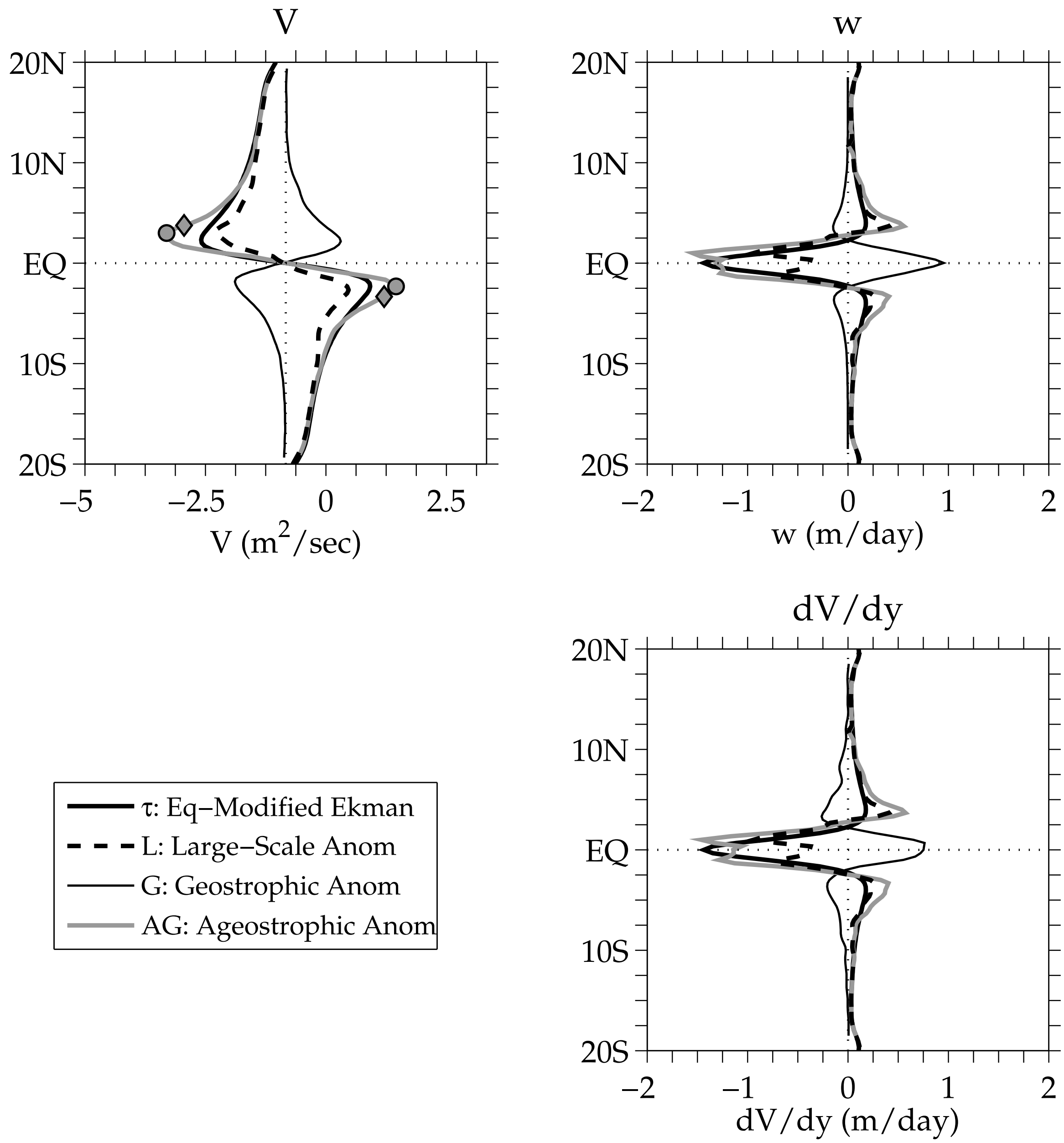

Figure 11. Weakened Trades run minus the control run during spring/summer along 140°W. 45-day mean depth-integrated meridional transport over upper 60 m, and w and $\frac{\partial V}{\partial y}$ at 60 m. Zonally low-pass filtered anomalies (dashed lines) are separated into geostrophic (thin black lines) and ageostrophic (gray lines) components and compared with equatorially-modified Ekman curves (thick black lines) from Fig. 4. Gray circles (diamonds) show extrema (inflection points) of mean V_{AG}.

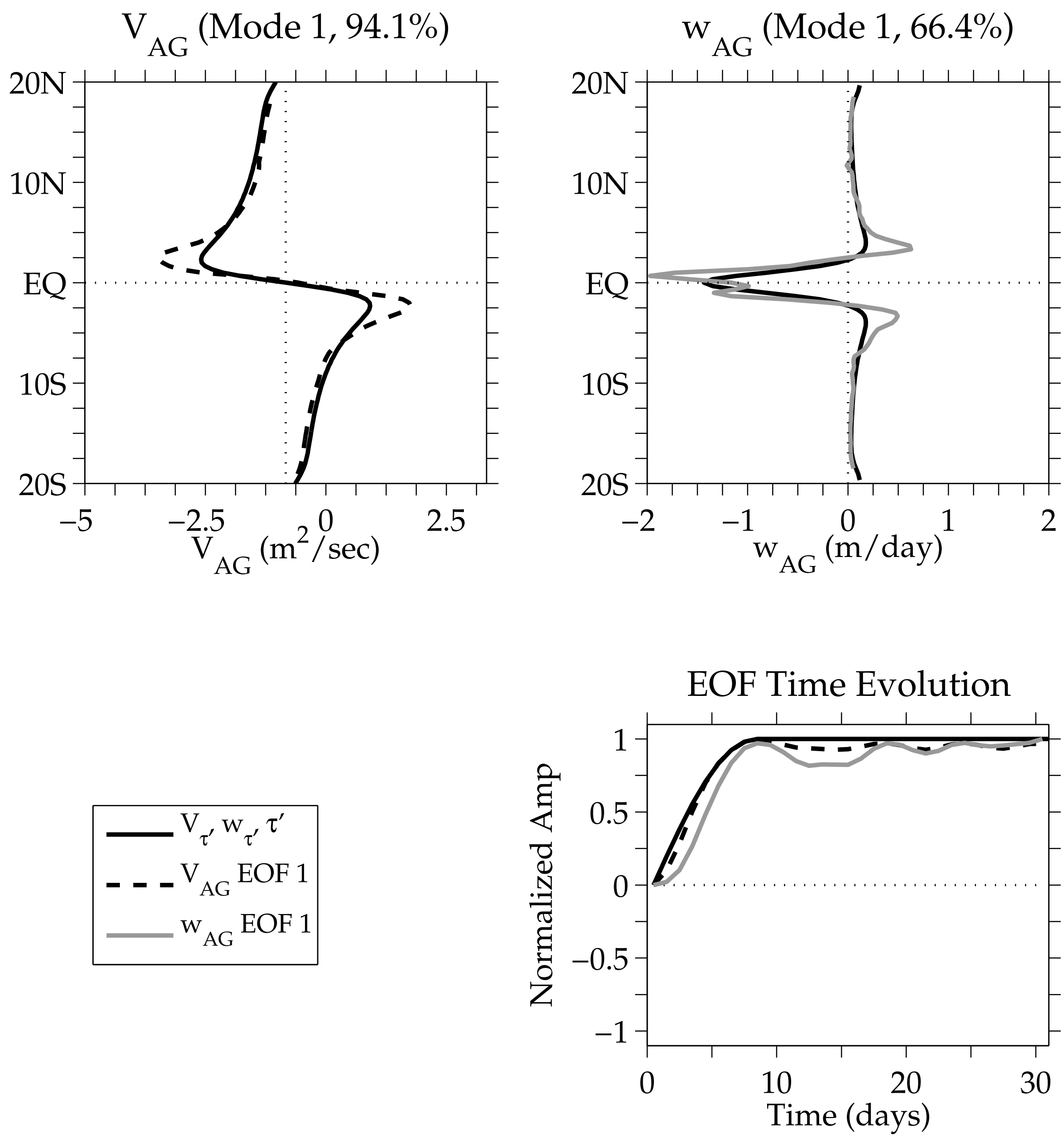

Figure 12. First EOF mode structure for V_{AG} (dashed line) and w_{AG} (gray line) along 140°W from weakened Trades run minus the control circulation during spring/summer. Percentage variance represented by first EOF provided on each panel. Thick black lines indicate corresponding equatorially-modified Ekman curves from Fig. 4. Lower right panel overlaps the temporal evolution of the westerly wind anomaly (thick black line) with the principle component time series of V_{AG} and w_{AG} (shifted to have zero origin).

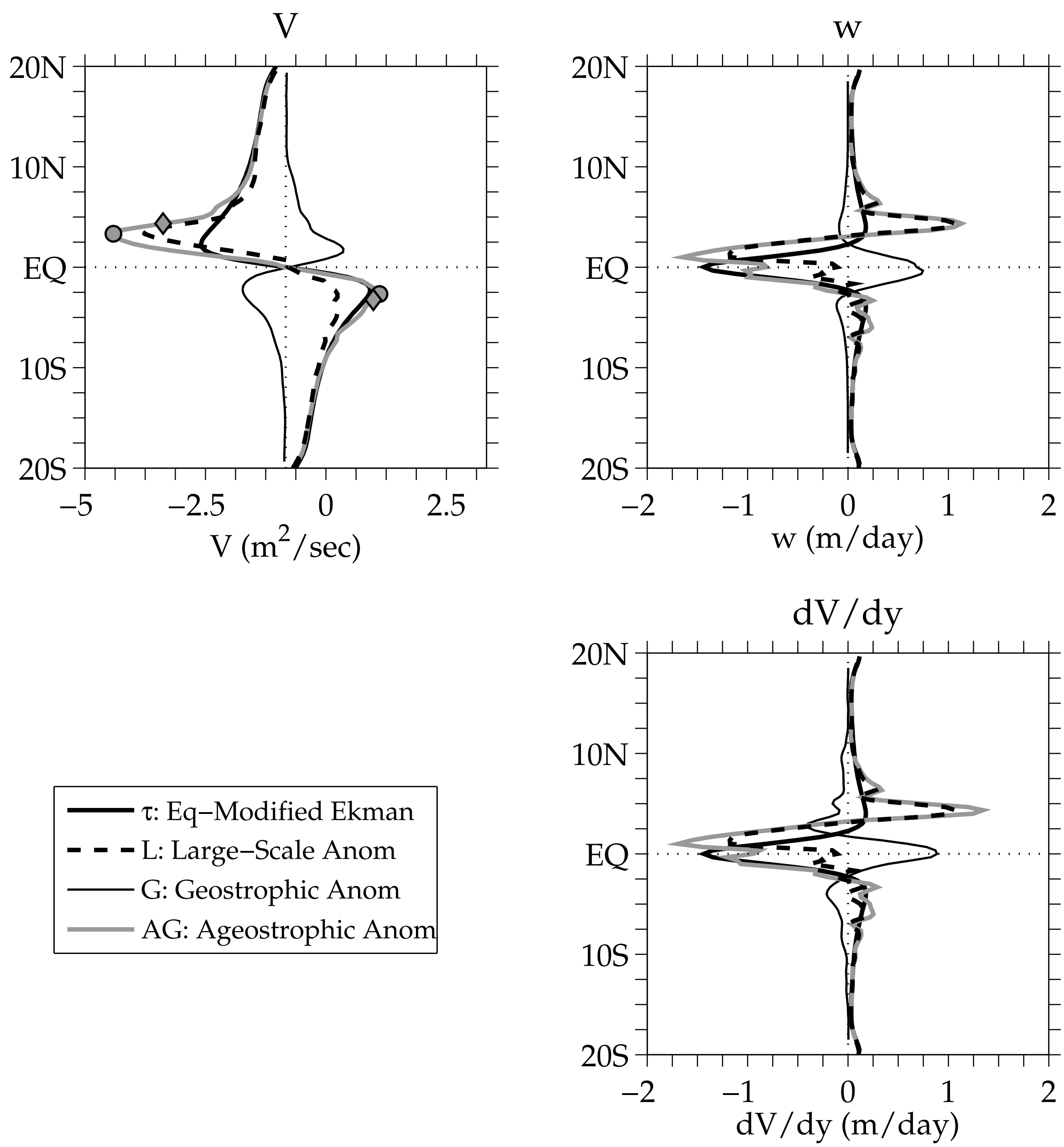

Figure 13. Weakened Trades run minus the control run during fall along 140°W. 45-day mean depth-integrated meridional transport over upper 60 m, and w and $\frac{\partial V}{\partial y}$ at 60 m. Zonally low-pass filtered anomalies (dashed lines) are separated into geostrophic (thin black lines) and ageostrophic (gray lines) components and compared with equatorially-modified Ekman curves (thick black lines) from Fig. 4. Gray circles (diamonds) show extrema (inflection points) of mean V_{AG}.

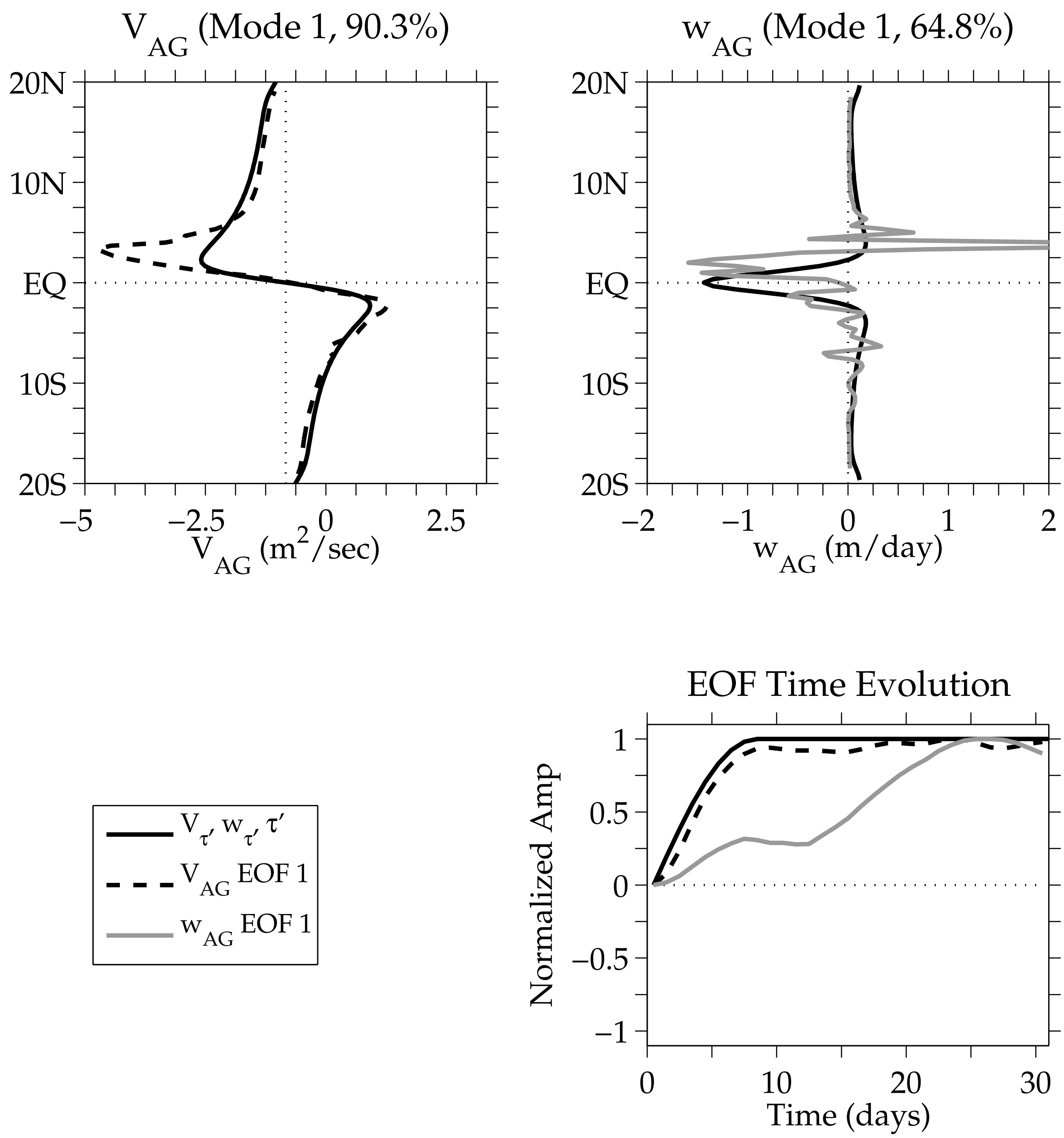

Figure 14. First EOF mode structure for V_{AG} (dashed line) and w_{AG} (gray line) along 140°W from weakened Trades run minus the control circulation during fall. Percentage variance represented by first EOF provided on each panel. Thick black lines indicate corresponding equatorially-modified Ekman curves from Fig. 4. Lower right panel overlaps the temporal evolution of the westerly wind anomaly (thick black line) with the principle component time series of V_{AG} and w_{AG} (shifted to have zero origin).

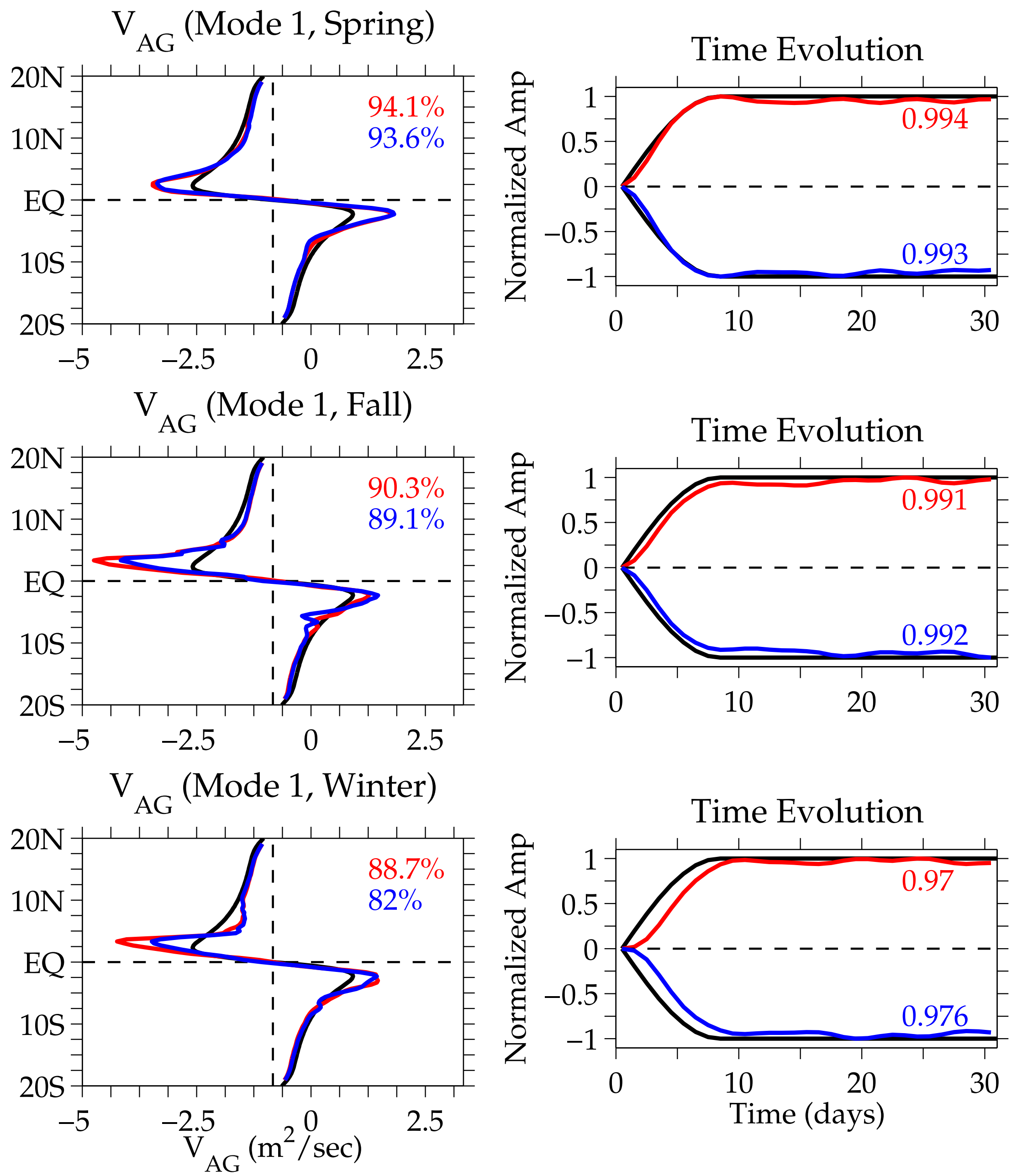

Figure 15. First EOF mode structure for V_{AG} along 140°W from strengthened Trades run minus the control circulation (blue line) during spring/summer, fall, and winter (left panels). Red and black lines indicate the corresponding curves for weakened Trades run V_{AG} and V_{τ} from Fig. 4, respectively. Percentage variance represented by first EOF provided on each panel. Right panels overlap the temporal evolution of the appropriate wind anomaly (black lines) with the principle component time series of V_{AG} (shifted to have zero origin). Zero-lag correlations with the wind anomaly are provided on each panel.

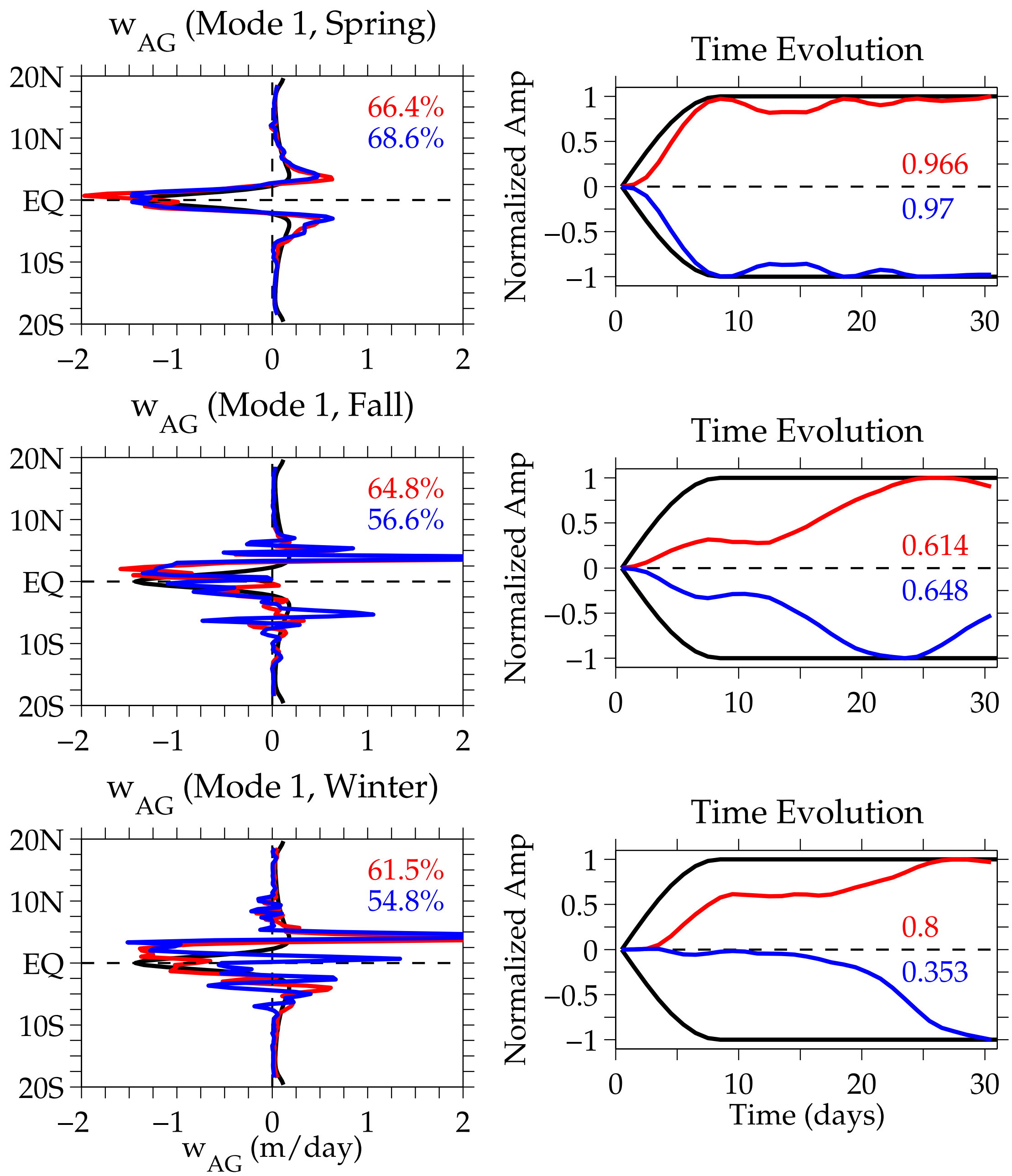

Figure 16. First EOF mode structure for w_{AG} along 140°W from strengthened Trades run minus the control circulation (blue line) during spring/summer, fall, and winter (left panels). Red and black lines indicate the corresponding curves for weakened Trades run w_{AG} and w_{τ} from Fig. 4, respectively. Percentage variance represented by first EOF provided on each panel. Right panels overlap the temporal evolution of the appropriate wind anomaly (black lines) with the principle component time series of w_{AG} (shifted to have zero origin). Zero-lag correlations with the wind anomaly are provided on each panel.

Table 1. Nomenclature.

Symbol	Description (section where symbol first appears)
$u_{clim}, v_{clim}, w_{clim}$	Velocity from climatological control run (section 2b)
$u_{total}, v_{total}, w_{total}$	Velocity from anomaly + climatological run (section 2b)
u, v, w	Anomalous velocity (section 2b)
u_g, v_g	Anomalous geostrophic velocity (section 2c)
u_{ag}, v_{ag}	Anomalous ageostrophic velocity (section 2c)
U_e, V_e, w_e	Ekman transport and vertical velocity (section 2d)
U_τ, V_τ, w_τ	Equatorially-modified Ekman transport and vertical velocity (section 2d)
r_s	Vertical shear dissipation rate (section 2d)
u_L, v_L, w_L	Zonally low-pass filtered anomalous velocity (section 2e)
V_L	v_L integrated over upper 60 m (section 3c)
V_G, w_G	Geostrophic component of V_L, w_L (section 3c)
V_{AG}, w_{AG}	Ageostrophic component of V_L, w_L (section 3c)

Table 2. Extrema, inflection points, and ratio of the magnitude of the northern extremum and southern extremum for the 45-day mean V_{AG} along 140°W. Mean ± standard deviation are reported for each season.

Season	S_{ext}	S_{infl}	N_{ext}	N_{infl}	$\lvert Ratio \rvert$
Spring	$2.17° \pm 0.19°$S	$2.94° \pm 0.32°$S	$2.83° \pm 0.33°$N	$3.68° \pm 0.72°$N	1.08 ± 0.03
Weak A	2.3°S	3.3°S	3.0°N	3.7°N	1.08
Strong A	2.0°S	2.9°S	3.0°N	4.2°N	1.12
Weak A*	2.3°S	2.9°S	2.3°N	2.6°N	1.10
Strong A*	2.0°S	2.6°S	3.0°N	4.1°N	1.04
Fall	$2.33° \pm 0.27°$S	$2.88° \pm 0.26°$S	$3.58° \pm 0.17°$N	$4.42° \pm 0.41°$N	1.61 ± 0.16
Weak A	2.7°S	3.3°S	3.3°N	4.3°N	1.84
Strong A	2.3°S	2.8°S	3.7°N	3.9°N	1.48
Weak A*	2.3°S	2.7°S	3.7°N	4.7°N	1.56
Strong A*	2.0°S	2.7°S	3.7°N	4.8°N	1.58
Winter	$2.92° \pm 0.69°$S	$3.52° \pm 0.70°$S	$3.58° \pm 0.17°$N	$4.23° \pm 0.19°$N	1.36 ± 0.16
Weak A	3.3°S	4.1°S	3.3°N	4.0°N	1.39
Strong A	2.3°S	2.8°S	3.7°N	4.4°N	1.12
Weak A*	3.7°S	4.1°S	3.7°N	4.2°N	1.46
Strong A*	2.3°S	3.1°S	3.7°N	4.3°N	1.47

A=0.025 N/m^2 and A*=A/10. Boldface indicates the two weakened Trades cases presented in section 3.

Table 3. r_s^{-1} computed from 45-day mean $w_{AG}(y = 0°\text{N})$, and location (S_{ext} and N_{ext}) and magnitude of 45-day mean V_{AG} extrema along 140°W. Mean ± standard deviation are reported for each season.

Season	$w_{AG}(y = 0°\text{N})$	S_{ext}	$V_A(y = S_{ext})$	N_{ext}	$V_A(y = N_{ext})$
Spring	1.99 ± 0.06	2.14 ± 0.19	2.57 ± 0.09	1.65 ± 0.22	2.78 ± 0.03
Weak A	1.91	1.98	2.61	1.54	2.81
Strong A	2.04	2.31	2.46	1.54	2.75
Weak A*	2.00	1.98	2.55	1.98	2.79
Strong A*	1.99	2.31	2.66	1.54	2.77
Fall	1.67 ± 0.26	2.00 ± 0.24	2.35 ± 0.09	1.29 ± 0.06	3.78 ± 0.24
Weak A	1.50	1.73	2.22	1.38	4.07
Strong A	2.03	1.98	2.37	1.26	3.50
Weak A*	1.46	1.98	2.40	1.26	3.73
Strong A*	1.68	2.31	2.43	1.26	3.83
Winter	2.01 ± 0.06	1.65 ± 0.38	2.41 ± 0.17	1.29 ± 0.06	3.26 ± 0.31
Weak A	1.96	1.38	2.56	1.38	3.55
Strong A	1.99	1.98	2.54	1.26	2.85
Weak A*	2.10	1.26	2.34	1.26	3.41
Strong A*	1.98	1.98	2.21	1.26	3.24

A=0.025 N/m^2 and A*=A/10. Boldface indicates the two weakened Trades cases presented in section 3.